

An X-ray survey of low-mass stars in Trumpler 16 with Chandra

J.F. Albacete-Colombo^{1,2}, F. Damiani², G. Micela², S. Sciortino², and F.R. Harnden, Jr.³

1- Centro Universitario Regional Zona Atlántica - Univ. COMAHUE, Monseñor Esandi y Ayacucho (CP 8500), Viedma, Argentina.

2- INAF-Osservatorio Astronomico di Palermo, Piazza del Parlamento 1, I-90134, Palermo, Italy.

3- AF Smithsonian Astrophysical Observatory, 60 Garden St., Cambridge, MA 02138, USA.

e-mail: albacete@fcaglp.unlp.edu.ar

Received —; accepted —

ABSTRACT

Aims. We identify and characterize low-mass stars in the ~ 3 Myr old Trumpler 16 region by means of a deep *Chandra* X-ray observation, and study their optical and near-IR properties. We compare X-ray activity of Trumpler 16 stars with known characteristics of Orion and Cygnus OB2 stars.

Methods. We analyzed a 88.4 ksec *Chandra* ACIS-I observation pointed at the center of Trumpler 16. Because of diffuse X-ray emission, source detection was performed using the PWDDetect code for two different energy ranges: 0.5–8.0 keV and 0.9–8.0 keV. Results were merged into a single final list. We positionally correlate X-ray sources with optical and 2MASS catalogues. Source events were extracted with the IDL-based routine ACIS-Extract. X-ray variability was characterized using the Kolmogorov-Smirnov test and spectra were fitted by using XSPEC. X-ray spectra of early-type, massive stars were analyzed individually.

Results. Our list of X-ray sources consists of 1035 entries, 660 of which have near-IR counterparts and are probably associated with Trumpler 16 members. From near-IR color-color and color-magnitudes diagrams we compute individual masses of stars and their A_v values. The cluster median extinction is $A_v = 3.6$ mag, while OB-type stars appear less absorbed, having $A_v = 2.0$ mag. About 15% of the near-IR counterparts show disk-induced excesses. X-ray variability is found in 77 sources, and typical X-ray spectral parameters are $N_H \sim 5.37 \times 10^{21} \text{ cm}^{-2}$ and $kT \sim 1.95 \text{ keV}$, with 1σ dispersions of 0.45 dex and 0.8 keV, respectively. OB stars appear, softer with a median $kT \sim 0.65 \text{ keV}$. The median X-ray luminosity is $6.3 \times 10^{30} \text{ erg s}^{-1}$, while variable sources show a larger median L_x value of $13 \times 10^{30} \text{ erg s}^{-1}$. OB-stars have an even higher median L_x of $80 \times 10^{30} \text{ erg s}^{-1}$, about 10 times that of the low-mass stars.

Conclusions. The Trumpler 16 region has a very rich population of low-mass X-ray emitting stars. An important fraction of its circumstellar disks survive the intense radiation field of its massive stars. Stars with masses $1.5\text{--}2.5 M_\odot$ display X-ray activity similar to that of stars in Cyg OB2 but much less intense than observed for Orion Nebula Cluster members.

Key words. stars: formation – stars: early-type – stars: pre-main-sequence individual: Trumpler 16 – X-rays: surveys – X-rays: stars.

On-line material: machine readable tables, color figures.

1. Introduction

The Carina nebula region (NGC 3372) is one of the most massive star formation regions of the Galaxy. It is associated with a giant HII region spanning about 4 deg² of the sky and being bisected by a prominent V-shaped dark gas and dusty lane. This prominent young structure is not as compact as some of the other young galactic clusters, but seemingly related to a spiral feature. In this direction, we are looking almost tangentially to the now recognized Carina-Sagittarius spiral arm, at the edge of a giant molecular cloud extending over about 130 pc and with a content in excess of 5×10^5 solar masses (Grabelsky et al., 1988). The concentration of massive stars (i.e. $M \geq 20 M_\odot$) interacts with the parent giant molecular cloud of the region, leading to triggered star formation events on intermediate to lower masses (e.g. Smith et al., 2004).

This region harbors several open clusters and/or star concentrations (Trumpler 14, 15 and 16; Collinder 228 and 232; Bochum 10 and 11) containing more than 60 known O-type stars (Feinstein, 1995). Large cavities within the giant molecular cloud are supposed to be carved out by the Tr 14 and 16 open clusters, which contain most of massive stars of the region. In particular Tr 16 includes three rare main-sequence O3 stars, the Wolf-Rayet (WR) star HD93162 and the famous luminous blue variable (LBV) η Carinae. There is a historical controversy about the distance and age of Tr 14 and Tr 16 (Walborn, 1995). For instance, from extensive spectroscopy and photometry Massey & Johnson (1993) find 3.2 kpc for both clusters. However, photometric studies are strongly affected by differential extinction in the region and peculiar reddening, and so the derived distance are different. An example is the Carraro et al. (2004) work, who for different $R = A_v / E(B-V)$ values (3.48 and 4.16 for Tr 16 and Tr 14 regions), compute

distances of 4.0 kpc and 2.5 kpc, respectively. A more reliable distance (2250 ± 180 pc), was derived from proper motion and Doppler velocities of the expanding η Carinae Homunculus using HST-STIS¹ observations (Davidson & Humphreys, 1997). Recent work (Tapia et al., 2003) derives a common distance $DM=12.14$ (2.7 kpc) and an age between ~ 1 Myr and 3 Myr, for Tr14 and Tr16, respectively. For this study, we adopt for Trumpler 16 a distance of 2250 pc and an age of 3 Myr. This young age agrees with the Smith et al. (2000) results, who report the existence of several embedded IR sources where star formation might be active. Also, DeGioia-Eastwood et al. (2001) confirm clear evidence of pre-main sequence (PMS) stars in the region, while Brooks et al. (2001) have identified two compact HII regions possibly linked to very young O-type stars. Finally, Hägele et al. (2004) report a compact cluster of infrared PMS-stars in Tr 16.

Of the existing methods to identify young stellar populations, the use of X-ray emission is perhaps the least biased (Feigelson et al., 2002). While in main-sequence (MS) stars, from late A to M dwarfs, X-rays are believed to originate from the hot coronal gas that is heated by stellar dynamo magnetic fields (Maggio et al., 1987), for late type Pre-MS stars (T-Tauri stars (TTSs)) X-ray emission is attributed to solar-like coronal activity but elevated by a factor of 10^3 - 10^4 (Feigelson & Montmerle, 1999). Several authors suggested the possibility of detecting early pre-main sequence (PMS) objects through their hard X-ray emission escaping the highly obscured regions (see Walter (1992); Kamata et al. (1997); Hofner & Churchwell (1997); Hofner et al. (2002)). Recently, X-ray surveys have been successful in identifying the young and pre-MS population in star-forming regions, including: *i*—deeply embedded Class I young stellar objects (YSOs), *ii*—low-mass T-Tauri PMS stars, *iii*—intermediate-mass Herbig Ae/Be PMS stars, *iv*—zero-age MS stars. Moreover, X-ray emission from low-mass pre-MS stars usually exhibits a strong variability that helps to confirm membership.

On last decade, X-ray observations of young stars on star-forming regions were intensified thanks to the high spatial resolution and the improved broad-band ([0.2-12.0] and [0.5-10.0] keV) effective area of the *XMM-Newton* and *Chandra* satellites. A first X-ray survey in the Carina region by Albacete Colombo et al. (2003) was performed on the basis of two early *XMM-Newton* observations (rev #115 and #116) centered on η Carinae . Because of the spatial resolution of the EPIC² camera and relatively short exposure time of the observations (~ 35 ksec), they detected only 80 X-ray sources, most of them related to the massive OB-type stars with $L_x \sim 10^{32}$ - 10^{34} erg s $^{-1}$. Before the observation used here, three *Chandra* observations were obtained on this region, two (obsId 50 and 1249) in the timed exposure mode, and the third (obsId 51) in the continuous clocking mode, which produces no image. Using only observation obsId 1249, Evans et al. (2003) presented luminosities and hardness ratios of the hot stars in Tr 16,

¹ Data from Hubble Space Telescope (HST) with the Space Telescope Imaging Spectrograph (STIS)

² European Photon Image Camera has about six times less spatial resolution than *Chandra* ACIS-I camera.

and part of Tr 14. Low-resolution X-ray spectra of luminous sources were discussed by Evans et al. (2004). However the short exposure time of such observation (~ 9.5 ksec) was a serious limitation for the study of intermediate- and low mass stellar population of the region. This limitation exists even if obsId. 50 and obsId. 1249 are combined (Sanchawala et al., 2007), reaching completeness just at X-ray luminosity (L_x) of $\sim 7 \times 10^{31}$ erg s $^{-1}$, i.e. the X-ray emission level typical of single O- and early B-type stars.

In this paper we present results of the analysis of the deepest X-ray observation ever done in this region (~ 90 ksec). Section 2 gives details on the observation and data reduction procedures. Section 3 explains the method used to detect the sources, photon extraction and the construction of the catalog. In section 4 we present results of the cross-correlation with existing near-IR and optical catalogs of objects and their characterization based on their color-color (CC) and color-magnitude (CM) diagrams. Section 5 presents a statistical study of variability in the X-ray domain. Section 6 is dealing with results of the analysis of extracted X-ray spectra. In section 7 we discuss X-ray luminosities of stars and compare them statistically with the X-ray source population of ONC and Cygnus OB2 star forming regions. In section 8 we discuss X-ray and stellar parameter of O- and early B- type stars. Finally, in section 9 we give a summary and draw conclusions of the paper.

2. X-ray observations

Trumpler 16 was observed with the ACIS detector on board the *Chandra X-ray Observatory* (CXO) (Weisskopf et al., 2002) on 2006 August 31³ (obsId 6402), as part of the *Guaranteed Time Observation* (GTO) *Chandra* program. The total effective exposure time was 88.4 ksec. The data were acquired in VERY FAINT mode, to ease filtering of non-X-ray events, with six CCD turned on, the four comprising the ACIS-I array [0,1,2,3], plus CCDs 6 and 7, part of ACIS-S. However, data from the latter two CCDs will not be used in the following because of the much degraded point spread function (PSF) and reduced effective area resulting from their large distance from the optical axis. The ACIS-I 17'' \times 17'' field of view (FOV) is covered by 4 chips each with 1024 \times 1024 pixels (scale 0.49'' px $^{-1}$). The observation was pointed toward R.A.=10^h 44^m 47.93^s and DEC=-59° 43' 54.21'', chosen to maximize the number of stars in the FOV and close to the optical axis, but also including most of the OB stars of the cluster. Figure 1-left shows Trumpler 16 as seen in X-rays by our ACIS-I observation.

Most of the observed X-ray sources in Fig.1-left are likely located toward the central part of Trumpler 16, spatially constrained by the dark V-shaped dust lane of the Carina region (Brooks et al., 1998). However, note the small X-ray source concentration inside this dark structure, located towards the South-East part of Fig 1. Deep near-IR observation are needed to reveal counterparts of such population. We defer to a forthcoming paper the use of some public HST - WFPCII⁴ obser-

³ Observation start date is JD 273350372.4528.

⁴ Hubble Space Telescope - Wide Filed Planetary Camera 2

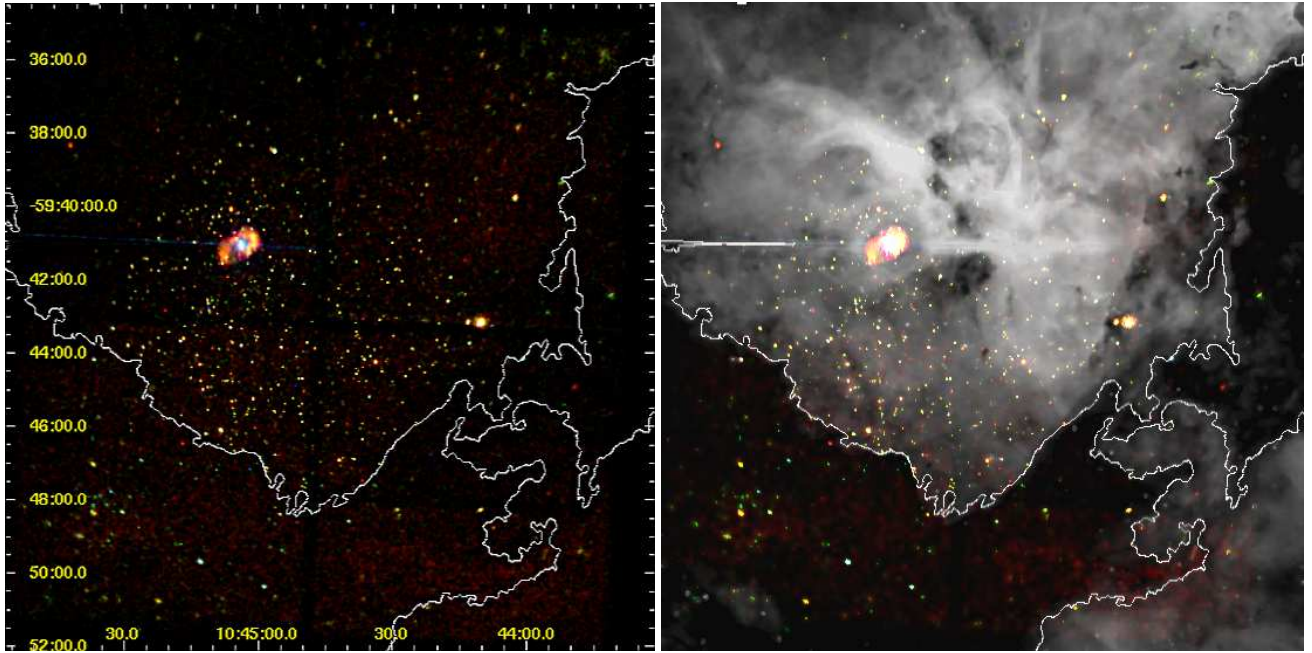


Fig. 1. Left: Color-coded ACIS-I image of the $17' \times 17'$ field in Trumpler 16 (see color version in the electronic edition). Kernel smoothing was applied to highlight point sources. Energy bands for the RGB image are [0.5:1.5], [1.5:2.2], and [2.2:8.0] keV for the red, green, and blue colors, respectively. Contour lines show the spatial distribution of the dark V-shaped dust lane. Right: ACIS-I image composed with a H_{α} image. This image clearly shows the sharp cut, along the V-shape structure, in the spatial distribution of X-ray sources.

vations to find signatures of star-environment interactions for some of the X-ray sources.

2.1. Data reduction

Data reduction, starting with the Level 1 event list provided by the pipeline processing at the CXO, was performed using CIAO 3.3.0.1⁵ and the CALDB 3.1.0 set of calibration files. We produced a level 2 event file using the `ACIS_PROCESS_EVENT` CIAO task, taking advantage of the VF-mode enhanced background filtering, and retaining only events with `grades = 0,2,3,4,6` and `status=0`. Photon energies were corrected for the time dependence of the energy gain using the `corr_tgain` CIAO task. Intervals of background flaring were searched for, but none were found. We will hereafter assume a non-variable background. To improve the sensitivity to faint sources, given the spectrum of the background and that of typical sources, we filtered out events outside the [500:8000] eV energy band.

3. Data analysis

We built images in the three band-passes 0.5-1.5 keV (soft), 1.5-2.2 keV (medium) and 2.2-8.0 keV (hard). Before the color-coded image combination, we corrected single band-images by variations in exposure, sensitivity and vignetting, by computing and dividing by its respective exposure maps. We construct a color-coded X-ray image of the region by composition of the three soft (red), medium (green) and hard (blue) images (see Fig. 1). This image is a 17×17 arcmin field which

comprises the center of Tr 16 and marginally the southeast part of Tr 14. In addition to revealing a huge number of X-ray point-like sources with different color-energies, inspection of Fig. 1 suggests the presence of soft diffuse X-ray emission in the region. In particular, Townsley (2006) use a 57 ksec ACIS-I observation centered on Tr 14 to study the diffuse X-ray emission in such a region and in the North-West part of Tr 16. They explain the diffuse X-ray emission as likely arising from the fast O-star winds that shock and thermalize the surrounding medium. Because homogeneous data analysis techniques are required to do justice to a comparison of diffuse X-ray emission in this data-set with that of Tr 14, this study will be presented in a forthcoming paper.

3.1. X-ray source detection

Source detection was performed with the Palermo Wavelet Detection code, PWDetect⁶ (Damiani et al., 1997b). It analyzes the data at different spatial scales, allowing the detection of both point-like and moderately extended sources, and efficiently resolving close source pairs. The most important input parameter is the detection threshold (SNR), which we establish from the relationship between background level of the observation and expected number of spurious detections due to Poisson noise⁷.

Diffuse soft (~ 0.2 -1.2 keV) X-ray emission has already been identified in this region (Corcoran et al., 1995; Townsley,

⁶ See http://www.astropa.unipa.it/progetti_ricerca/PWDetect

⁷ This last quantity was determined from extensive simulations of source-free fields (see Damiani et al., 1997a)

2006) and causes different (non-uniform) X-ray background levels across the FOV of our observation. The best way to reduce the diffuse emission contribution is to discard soft photons in the detection procedure. We compute background (BKG) levels in four different energy ranges: 0.5-8.0 keV, 0.7-8.0 keV, 0.9-8.0 keV and 1.1-8.0 keV. Since exposure maps are needed by the source detection algorithm, we used event files in these energy bands as input to the CIAO tool MKEXPMAP and assumed a monochromatic spectrum ($kT=2.0$ keV)⁸. The background level for each energy band was computed as the average of values measured in three circular regions free of sources. If we accept 10 spurious detections in the ACIS FOV⁹, mean computed background levels can be translated into different SNR thresholds for each energy band, i.e.: 4.7, 4.65, 4.6 and 4.55, respectively. These input parameters for PWDetect result in different numbers of detected sources in each energy band, for instance, 1266 sources in the 0.9-8.0 keV band, greater than detected in the "canonical" 0.5-8.0 keV band (1214 sources). This is consistent with the effect of diffuse soft X-ray emission in masking weak sources.

A careful visual inspection was performed on the 0.5-8.0 keV and 0.9-8.0 keV source lists. We manually rejected respectively 242 and 271 detections, considered spurious either because they were produced by different instrumental artifacts (e.g. CCD gaps, detector edges, false detections along the read out trails), or since they resulted from the "fragmentation" into discrete sources of the extended emission making a toroidal ring around the LBV star η Carinae (Fig. 1). Furthermore examination of afterglow¹⁰ contamination led us to discard 29 and 20 false detections, respectively. The final source list was constructed by merging both catalogues: the list of 943 sources detected in the 0.5-8.0 keV band and the 1004 sources detected in the 0.9-8.0 keV band. Merging was performed using a criterion of maximum detection significance. The two catalogues coincide in 798 sources, consisting of 322 sources with $Sig_{0.5-8.0} > Sig_{0.9-8.0}$, while for the remaining 476 sources $Sig_{0.9-8.0} > Sig_{0.5-8.0}$ (where Sig_{x-y} is the detection significance in the $x-y$ energy band). Sixty-one sources were detected only in the 0.5-8.0 keV band, while 176 are exclusive to the 0.9-8.0 keV band and would have otherwise remained hidden because of the diffuse emission. This procedure led to a total number of 1035 X-ray sources in the entire field, which we analyze here.

3.2. Photon extraction

Even with the high spatial resolution of the *Chandra* ACIS-I camera, the high source density in Trumpler 16, source photon extraction is not an easy task. Although circular regions would contain a relatively large fraction of the PSF for almost all source photons, the extended wings of the PSF mean that very large regions would be needed, incurring in the risk of contamination from nearby sources. Moreover, the resulting inclusion

of a large number of background events would reduce the signal to noise of weak sources. On the other hand, extraction from regions that are too small may reduce the photon statistics for further spectral and timing analysis. To address these issues, we decided to use ACIS EXTRACT (AE) v3.79 (Broos et al., 2002), an IDL based package that makes use of TARA¹¹, CIAO and FTOOLS¹² software.

This task reduces the problem of accounting for non-Gaussian shapes of the local PSF by calculating the shape of the PSF model at each individual source's position. For some sources the background level is affected by the extended PSF wings of the bright sources (η Carinae and WR25) in the FOV. AE computes source background locally, by defining background extraction regions as circular annuli with inner radii 1.1 times the maximum distance between the source and the 99% PSF contour, and outer radii defined so that the regions contain more than 100 "background" events. In order to exclude contamination of the regions by nearby sources, background events are taken from a "Swiss cheese" image that excludes events within the inner annuli radii of all the 1035 sources.

AE source extraction was performed using a PSF model that contains a specified fraction of source events (f_{PSF}). Generally, we choose $f_{PSF}=90\%$, and computed the contours from the PSF for a mono-energetic source with $E = 1.49$ keV. For 9.9% of the sources in the denser parts of the Trumpler 16 field this fraction was reduced to avoid contamination with other nearby sources, in the most extreme cases down to $f_{PSF}\sim 50\%$ (just 3 sources).

Following AE science hints, we then refine the initial source positions computed by PWDetect¹³ by correlating the source images with the model of local PSF computed by AE libraries. This procedure was only used for those sources lying at off-axis larger than 5 arcmin (316 sources), while for the rest of the source (719 sources) we simply adopt mean photon positions¹⁴. AE also estimates local background spectra, computes redistribution matrix files (RMFs) and auxiliary response files (ARFs), constructs light curves, performs Kolmogorov-Smirnov variability tests, and computes photometry in 14 different energy bands. Results of AE procedure appears in Table 1, which lists source number in column (1), name according to CXC naming convention¹⁵ (2), sky position (R.A. and Dec. J2000) (3,4) with relative uncertainty (5), off-axis angle (θ) (6), significance of the detection (Sig.) from PWDetect analysis (7), the source extraction area (8); the PSF fraction within the extraction area, assuming $E=1.49$ keV (9); the background-corrected extracted source counts in the 0.5-8.0 keV band (NetCnts) (10); the count rates (CR = NetCnts/Exptime/PSF_{frac}) in three spectral bands: 0.5-8.0 keV, 0.5-2.0 keV and 2.0-8.0 keV, (11-13); source photon quantiles at 25, 50 and 75% percent in columns 14 to 16 (see sub-section 3.3), the median photon energy (\bar{E}_x) in (17).

⁸ http://asc.harvard.edu/ciao/download/doc/expmap_intro.ps

⁹ See reasons of this choice in Albacete Colombo et al. (2007).

¹⁰ Afterglow is defined as the residual charge from the interaction of a cosmic ray with the CCD. If afterglow events are not removed from the data, they can result in the spurious "detection" of faint sources.

¹¹ <http://www.astro.psu.edu/xray/docs/TARA/>

¹² <http://heasarc.gsfc.nasa.gov/docs/software/ftools/>

¹³ PWDetect assumes a symmetric PSF.

¹⁴ Please follow Acis-Extract technical procedures at website http://www.astro.psu.edu/xray/docs/TARA/ae_users_guide

¹⁵ <http://cxc.harvard.edu/cdo/scipubs.html>

Table 1. Trumpler 16 X-ray source catalog (see the electronic version for the complete table).

N _x #	NAME CXO J+	R.A	DEC.	Error	θ	Sig.	Area	PSF	Cts	Count Rates ($\times 10^{-3}$ cnt s ⁻¹)			Quantiles	E_x	Var.	flag.		
		[h:m:s]	[d:m:s]	(")	(σ)	(px.)	(%)	(ph.)	Tot.	Soft	Hard	Q ₂₅	Q ₅₀	Q ₇₅	(keV)	log(P _{ks})	id	
1	104338.73-593832.7	10:43:38.74	-59:38:32.74	0.57	10.24	4.62	1757	0.90	30	0.392	0.311	0.081	0.12	0.10	--	1.28	-0.38	-1
2	104341.39-594538.8	10:43:41.39	-59:45:38.81	0.53	8.56	6.03	1024	0.90	36	0.458	0.372	0.086	0.08	0.10	0.58	1.22	-0.16	-1
3	104341.41-594224.5	10:43:41.41	-59:42:24.52	0.28	8.52	16.38	964	0.91	208	2.626	1.533	1.093	0.13	0.17	0.37	1.74	-0.39	-2
4	104341.48-594102.2	10:43:41.49	-59:41: 2.26	0.43	8.86	6.15	997	0.90	55	0.704	0.448	0.256	0.07	0.10	0.38	1.25	-1.31	-2
5	104343.14-594409.0	10:43:43.15	-59:44: 9.02	0.46	8.17	5.88	726	0.90	28	0.361	0.052	0.309	0.23	0.24	--	2.31	-0.39	-1
6	104343.98-594655.9	10:43:43.99	-59:46:55.93	0.43	8.60	4.83	843	0.90	41	0.532	0.483	0.049	0.11	0.09	0.55	1.19	-0.76	-4
7	104344.11-594817.9	10:43:44.11	-59:48:17.95	0.46	9.16	5.29	1042	0.90	47	0.602	0.550	0.052	0.08	0.07	0.56	1.01	-1.05	-1
8	104345.36-593948.7	10:43:45.37	-59:39:48.78	0.36	8.89	7.30	731	0.89	54	0.699	0.498	0.201	0.11	0.10	0.31	1.25	-0.34	-2
9	104345.37-593847.5	10:43:45.37	-59:38:47.54	0.40	9.40	5.83	970	0.91	45	0.580	0.227	0.353	0.14	0.11	0.49	1.36	-2.29	-1
10	104345.44-594158.9	10:43:45.44	-59:41:58.95	0.44	8.11	5.31	564	0.90	25	0.321	0.150	0.171	0.14	0.15	0.43	1.63	-0.11	-1
11	104346.39-594929.8	10:43:46.39	-59:49:29.82	0.37	9.55	4.72	474	0.74	41	0.634	0.550	0.084	0.11	0.10	0.35	1.22	-0.74	-1
12	104348.15-594924.4	10:43:48.15	-59:49:24.41	0.29	9.32	12.27	927	0.91	132	1.677	1.276	0.402	0.12	0.10	0.35	1.28	-1.24	-2
13	104349.40-594456.3	10:43:49.41	-59:44:56.36	0.28	7.45	13.68	418	0.90	89	1.138	1.118	0.020	0.06	0.06	0.56	0.98	-0.96	-3
14	104350.13-594552.6	10:43:50.14	-59:45:52.69	0.47	7.54	5.11	427	0.90	15	0.203	0.248	0.044	0.08	0.07	--	1.01	-0.36	-1
15	104350.71-593744.4	10:43:50.71	-59:37:44.45	0.42	9.49	5.21	905	0.89	41	0.539	0.414	0.125	0.12	0.11	0.47	1.33	-0.78	-4
16	104350.89-595031.2	10:43:50.90	-59:50:31.25	0.39	9.76	5.26	1073	0.90	23	0.302	0.164	0.138	0.16	0.09	0.68	1.15	-2.67	-4
17	104351.09-594024.6	10:43:51.10	-59:40:24.67	0.38	7.97	5.42	479	0.89	28	0.361	0.239	0.122	0.11	0.09	0.36	1.20	-0.31	-1
18	104351.64-594525.1	10:43:51.64	-59:45:25.10	0.40	7.25	7.05	376	0.90	31	0.400	0.253	0.147	0.14	0.16	0.39	1.72	-3.15	-2
19	104351.87-594035.6	10:43:51.88	-59:40:35.60	0.43	7.81	5.87	443	0.89	7	0.102	0.102	0.001	0.13	0.09	--	1.21	-0.34	-2
20	104352.13-594802.0	10:43:52.13	-59:48: 2.00	0.40	8.15	5.23	528	0.90	30	0.388	0.239	0.149	0.12	0.09	0.37	1.16	-0.46	-4
21	104352.25-594157.6	10:43:52.25	-59:41:57.68	0.39	7.28	5.31	357	0.89	25	0.325	0.301	0.023	0.07	0.08	0.93	1.07	-0.16	-4
22	104352.48-593920.9	10:43:52.48	-59:39:20.96	0.23	8.35	19.14	592	0.90	176	2.250	1.401	0.849	0.13	0.16	0.39	1.70	-0.50	-2
23	104354.13-594145.2	10:43:54.14	-59:41:45.24	0.37	7.11	4.81	357	0.90	25	0.325	0.101	0.224	0.09	0.15	0.38	1.63	-0.17	-1
24	104354.20-593805.2	10:43:54.21	-59:38: 5.24	0.41	8.93	5.21	737	0.89	22	0.290	0.196	0.094	0.15	0.12	0.72	1.43	-0.52	-1
25	104355.11-593624.2	10:43:55.11	-59:36:24.23	0.30	10.04	13.22	1205	0.90	177	2.246	1.378	0.869	0.13	0.15	0.37	1.59	-4.00	-2
26	104355.14-594750.4	10:43:55.14	-59:47:50.42	0.35	7.72	7.89	451	0.90	44	0.567	0.470	0.097	0.07	0.08	0.50	1.07	-1.07	-3
27	104355.47-594253.5	10:43:55.48	-59:42:53.59	0.29	6.69	13.04	278	0.89	51	0.664	0.357	0.306	0.14	0.17	0.53	1.74	-3.51	-2
28	104355.56-594923.0	10:43:55.57	-59:49:23.07	0.30	8.57	8.43	629	0.90	77	0.989	0.807	0.182	0.09	0.08	0.35	1.13	-0.50	-2
29	104356.25-594936.4	10:43:56.25	-59:49:36.48	0.33	8.65	5.36	648	0.89	36	0.471	0.335	0.136	0.14	0.09	0.39	1.21	-0.41	-1
30	104356.82-594236.0	10:43:56.82	-59:42:36.03	0.46	6.57	4.90	257	0.89	12	0.158	0.139	0.019	0.12	0.12	--	1.41	-0.41	-1

Notes: Column labeled with θ refers to the off-axis angle measured in arcmin from the aim point of the observation. Sig. is the significance of the source in number of sigma over background. Flag Id = -1: sources detected only in the 0.9-8.0 keV band. flag Id = -2 and -3 correspond to sources detected in both bands, but $\text{Sig}_{0.9-8.0} > \text{Sig}_{0.5-8.0}$ and $\text{Sig}_{0.9-8.0} < \text{Sig}_{0.5-8.0}$, respectively. Flag Id = -4 refers to sources detected only in the 0.5-8.0 keV band.

Column 18 is the $\log(P_{ks})$ Kolmogorov-Smirnov probability of non-variability (see section § 5), and in (19) are flags from PWDetect detection code.

3.3. X-ray hardness ratios

A commonly used tool to explore the spectral properties of sources with low photon statistics is the hardness ratio (e.g. Schulz et al., 1989; Prestwich et al., 2003). In this conventional method, the full energy range is divided into two or three sub-bands and the detected source photons are counted separately in each band. Most popular definitions for a single hardness ratio (HR) exists on basis of only two energy sub-bands: *i*– HR=H/S or *ii*– HR=(H-S)/(H+S). By these definitions, HR is very sensitive to small changes (i.e. statistical fluctuations) in the number of photons falling in each band. The requirement of total counts in the full energy band is at least 40 photons (just 36% of our sources satisfy this constraint). Above this limit HR becomes a "reliable method" to estimate the real hardness of sources (Albacete Colombo et al., 2007).

An improved method to resolve this limitation is based on the quantile analysis (Hong et al., 2004). Instead of working with predetermined energy bands, we determine the energy E^x below which the net counts is $x\%$ of the total counts of the source. We define quantile Q_x as: $\frac{E^x - E_{\min}}{E_{\max} - E_{\min}}$, where in our study $E_{\min}=0.5$ keV and $E_{\max}=8.0$ keV. We compute median Q_{50} values and quartiles Q_{25} and Q_{75} and give values in Table 1. A minor inconvenience of this method is that for a given spectrum, various quantiles cannot be considered independent variables, unlike the counts in different energy bands. However, Hong et al. (2004) overcome this problem by considering the $\log(Q_{50}/(1-Q_{50}))$ vs. $3(Q_{25}/Q_{75})$ plane. Based on an extensive set of simulated spectra, they predict loci of models in this plane. We use a set of absorbed thermal models with plasma temperatures of 0.2, 0.5, 1, 2, 4, 10 keV and N_H equal to 10^{20} , 10^{21} , 0.4×10^{22} , 10^{22} , 4×10^{22} and 10^{23} cm $^{-2}$. Note that the spectrum changes from soft to hard as one goes from left to right in the diagram (see Fig. 2).

In a statistical sense, a comparison between sources in the grid models suggest typical N_H and kT values distributed around 0.8×10^{22} cm $^{-2}$ and 1.5 keV, but dispersed within grid models of $N_H=0.4-1.0 \times 10^{22}$ cm $^{-2}$ and $kT=1-3$ keV, respectively. The absence of a systematic difference between the position of sources with and without a 2MASS identification on the hardness-ratio plane is likely to a combination of two observational bias: *i* related to the limiting magnitude of the 2MASS photometry ($K_s^{\text{limit}} \sim 14.3$ mag.); *ii* the X-ray sensitivity of the *Chandra* data ($f_x^{\text{limit}} \sim 10^{-14.5}$ erg s $^{-1}$ cm $^{-2}$). However is not clear, from the observational point of view, i.e. through the near-IR and X-ray flux source distributions, that a fraction of faint stellar X-rays sources would not have 2MASS counterparts. Deeper near-IR and X-ray observations are needed to unveil this issue.

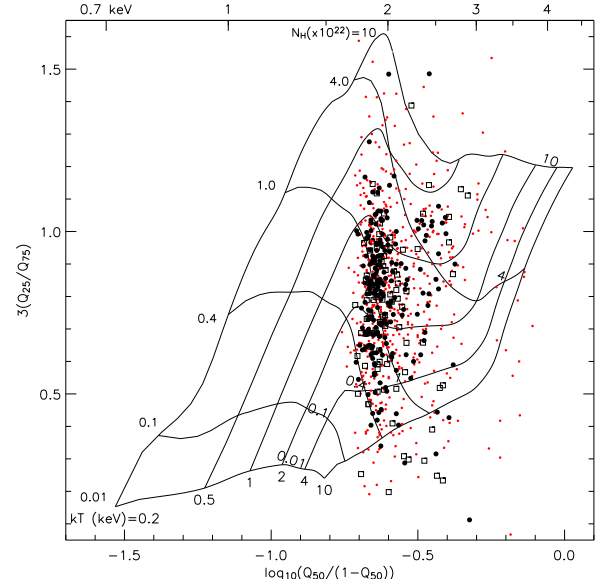


Fig. 2. Quantile Color-Color Diagram (QCCD). The energy scale in the top X-axis shows the median energy values (Q_{50}). The grid pattern represents the location of simulated spectra in the diagram (Hong et al., 2004). Note: *Filled circles* and *open boxes* refer to X-ray sources with and without 2MASS counterparts (see next section), respectively. *Small dots* (red) correspond to sources with unreliable quantile values affected by poor photon statistics (≤ 10 photons).

4. Optical and near-IR analysis

4.1. Counterparts

The large amounts of gas, dust and selective extinction of the region, combined with the absence of available deep ($V > 19$ mag) optical photometry, prevent finding optical counterparts for most of our X-ray sources. We consider it appropriate only to use optical data to identify the massive star population (typical $V < 12$, Massey & Johnson (1993)) of the region (i.e. Wolf-Rayet, O- and early B-types). We use a recent compendium of massive stars in the Carina Nebula presented by Smith (2006). Out of a total of 60 stars, 44 lie within the 0.0823 deg 2 FOV of our X-ray observation. We added the binary (O5.5V + O9.5V) FO 15 (Niemela et al., 2006), not included in the list of Smith (2006). Our final list of 45 hot massive stars is comprised of: 1 LBV, 1 Wolf-Rayet, 21 O-type stars and 22 early B-type stars. With a cross-identification radius of 3 arcsec, a total of 28 X-ray sources were identified. All the O-type stars were identified as X-ray emitters, while just 7/22 (~31%) of early B-type (SpT. between B0V to B1.5V) have detectable X-ray emission. The list of massive stars with X-ray counterparts and the discussion of their X-ray properties is presented in § 8.

Apart from the massive stars, our X-ray population is essentially composed of low-mass stars. In such a young cluster like Tr 16, low-mass stars are often optically invisible, being embedded and/or obscured by high amounts of gas and dust. We partially solve this problem by use of the near-IR observations, on which the impact of dust extinction is reduced. We adopt

J ($1.25\text{ }\mu\text{m}$), H ($1.65\text{ }\mu\text{m}$) and K_s ($2.17\text{ }\mu\text{m}$) photometry from the *Two Micron All Sky Survey* (2MASS) Point Source Catalog (PSC)¹⁶. 2MASS is complete to magnitudes of 15.8, 15.1 and 14.3 mag in the J , H and K_s bands, respectively. We restricted our photometry analysis to 2MASS sources with flag quality A, B, C or D in at least one of the three magnitudes (see explanation in the 2MASS All-Sky Data Release User's Guide). With this restriction 20 sources were removed from our initial list of 5938 sources in the ACIS FOV of our observation. This leaves a total of 5918 2MASS objects¹⁷.

We began by cross-identifying our X-ray source list with the 2MASS catalog. Identification radii, R_{id} , were chosen to limit the number of spurious identifications due to chance alignments, N_{chance} , and at the same time to include a large number of the true physical associations, N_{true} . Identification radii used were 1.0, 1.5, 2.1, and 2.7 arcsec adopted for the four different off-axis angle ranges: [0-2), [2-4), [4-7) and > 7 arcmin, respectively¹⁸. Results of the final identification are presented in § 4.3 and shown in Table 2. The first seven columns are: X-ray source number; 2MASS nomenclature for identified sources; the offset between the two positions; J , H , K_s magnitudes; photometry quality flag (Ph.Q); confusion flag (Cont). A total of 660 X-ray sources out of the 1035 in our list were identified with 665 2MASS objects. Five X-ray sources (#96, #382, #401, #816 and #1034) were identified with two 2MASS counterparts each. After a visual inspection, we kept only the closer counterparts. Thus the final list of near-IR counterparts consists of 660 entries.

We estimate the expected number of extragalactic sources in our detection list by following Flaccomio et al. (2006) procedure. We consider the ACIS count-rates of non-stellar sources in the *Chandra Deep Field North* (CDFN, Alexander et al., 2003; Barger et al., 2003) and estimate absorption corrected count-rates assuming $N_H = 5 \times 10^{21}\text{ cm}^{-2}$ (from $A_V \sim 3.6$, see § 4.3) using PIMMS and assuming power-law spectra with index 1 and 2 (Giacconi et al., 2001). We then compare these count rates with upper limits taken at random positions in the ACIS FOV. For Γ between 1 and 2 we obtain 72 to 95 expected extragalactic sources. Given the intrinsic near-IR fluxes of these sources and the absorption toward Trumpler 16, they are expected to be among the 385 without NIR counterparts (cf. Flaccomio et al. 2006). This means that no more than 18 to 24% of the unidentified X-ray population is related to extragalactic sources.

4.2. Unidentified X-ray sources

A large population of young stars, proto-stars, deeply embedded in dense circumstellar gas and dust should be present in the Carina Nebula (Smith et al., 2003). However optical and near-IR counterparts of YSOs are difficult to detect. Fortunately, X-ray emission is expected in young stellar objects along all their

initial phases (Montmerle et al., 2000). X-ray photons easily escape from dense circumstellar material, where absorption process becomes important mainly for energies below 1.2 keV (Morrison & McCammon, 1983b). This makes hard X-ray energies the most appropriate "window" to detect counterparts of deeply embedded young sources.

Of the 375 X-rays sources without near-IR counterparts, just a small fraction ($\sim 20\%$) is expected to be extra-galactic contamination (see §4.1). We are thus dealing with about ~ 300 candidate young (first stage) low-mass stars, highly obscured by circumstellar material. In our data these sources typically have lower X-ray photon statistics than those with near-IR counterpart, i.e. ~ 8 vs. 28 average photons, respectively. In X-rays, no quantitative differences in the median energy and spectral quantiles were found for the X-ray sources with and without near-IR counterparts.

4.3. Near-IR properties of identified X-ray sources

We now investigate the near-IR properties of the X-ray sources. For this purpose we restrict our analysis to sources with high quality photometry ($Ph.Q=AAA$) and no confusion ($Cont.=000$). With these requirements the total number of IR sources in the ACIS FOV is reduced from 5918 to 2178. We have also set a further requirement on near-IR counterparts of X-ray sources, that their J , H , and K_s magnitude errors be all < 0.1 mag. All these requirements yield 367 X-ray sources with good near-IR counterparts, out of the original 660.

Figure 3 shows the $J-H$ vs. $H-K_s$ color-color (CC) diagram for these AAA-flagged sources. We also plot for comparison the MS (Kenyon & Hartmann, 1995), the Classical T-Tauri Stars (CTTS) locus of Meyer et al. (1997), and reddening vectors starting from these loci and with slope ($A_{K_s}/E(H - K_s) = 0.125$) corresponding to the extinction law given by Hanson (2003). Trumpler 16 members with purely photospheric emission should lie in this reddening band. Otherwise, Young stellar objects (YSOs), such as Classical T Tauri and Herbig Ae/Be stars, because of the NIR excess emission originating in the inner parts of their circumstellar disks, are often found to the right of this band, i.e. in the CTTS locus. Fifty-one (out of 367) X-ray sources, i.e. likely Trumpler 16 members, have colors consistent with the (reddened) CTTS locus. This means a fraction of 51/339 (28 OB stars were discarded) $\sim 15\%$ of all (low-mass) identified X-ray sources in the CC diagram. Of all 51 sources with intrinsic K -excess i.e. disk-star systems, eleven (Src-Id: 36, 41, 209, 230, 773, 966, 993, 996, 1002, 1003 and 1009) appears below the CTTS vectors, but with intrinsic bright K_s magnitudes, as is shown in both panels of Fig 4. They are probably intermediate- to high-mass young stars with an intrinsic K -band excess that would be produced by massive accretion disks and/or extended envelopes surrounding massive YSOs. If confirmed, they will contribute for about 40% of the total massive star population of the Trumpler 16 region.

Figure 4-left shows the K_s vs. $J-K_s$ color magnitude (CM) diagram for the same stars plotted in Fig. 3. We also show for reference the expected cluster locus: the intrinsic K_s magnitudes and $J-K_s$ colors for stars earlier than B5V were

¹⁶ See <http://www.ipac.caltech.edu/2mass>

¹⁷ We note that the 2MASS catalog appears to have a "hole" around η Carinae (~ 1.5 arcmin radius).

¹⁸ The adopted radii were computed following technical procedures presented in Albacete Colombo et al. (2007)

Table 2. Near-IR counterparts of Trumpler 16 X-ray sources. The complete version is available in the electronic edition of A&A.

N _x	2MASS J+	Offset (")	J mag.	H mag.	K _s mag.	Ph.Q	Cont.	A _v	Mass	Notes
1	10433859-5938306	2.33	14.57±0.03	13.21±0.04	12.63±0.03	AAA	000	7.93	2.05	
2	-----	--	-----	-----	-----	--	--	--	--	--
3	10434145-5942245	0.30	14.18±0.03	13.20±0.02	12.82±0.02	AAA	000	4.59	2.24	
4	10434126-5941002	2.62	15.47±--	15.31±0.14	14.60±0.14	UBB	000	--	--	
5	10434295-5944080	1.77	15.63±0.08	14.31±0.06	13.27±0.04	AAA	000	15.27	1.25	K-excess
6	-----	--	-----	-----	-----	--	--	--	--	--
7	10434401-5948177	0.76	8.70±0.02	8.51±0.04	8.47±0.02	AAA	000	1.38	19.2	O9.5V
8	10434538-5939468	1.92	15.90±--	14.88±--	14.90±0.16	UUC	000	--	--	
9	10434536-5938471	0.36	16.02±0.10	14.04±0.04	13.02±0.04	AAA	000	14.90	1.01	
10	10434525-5941567	2.61	14.37±0.06	12.99±0.05	12.18±0.04	AAA	000	12.05	2.16	K-excess
11	10434659-5949292	1.68	13.69±0.05	12.68±0.05	12.25±0.04	AEA	c0c	--	2.38	
12	10434809-5949246	0.50	13.51±--	13.09±0.07	12.85±0.05	UAA	0cc	--	--	
13	10434937-5944549	1.45	12.67±0.02	12.20±0.03	12.06±0.03	AAA	000	0.82	4.89	
14	10435007-5945530	0.59	15.56±0.05	14.59±0.03	14.19±0.07	AAA	000	4.31	1.30	
15	10435085-5937437	1.28	14.86±0.05	13.74±0.05	13.40±0.05	AAA	000	3.76	1.86	
16	10435088-5950307	0.47	12.20±0.02	11.99±0.03	11.88±0.02	AAA	000	0.28	6.22	
17	10435123-5940243	1.06	14.60±0.05	13.38±0.04	12.88±0.04	AAA	000	6.57	2.03	
18	10435132-5945239	2.64	15.54±0.08	14.06±--	13.55±--	AUU	cpp	--	1.31	
19	10435191-5940353	0.40	16.49±0.16	15.15±0.09	14.63±0.11	CAA	000	--	0.70	
20	10435186-5948017	2.02	14.49±0.05	13.46±0.06	12.95±0.05	AAA	000	6.60	2.09	
21	10435223-5941574	0.29	14.83±0.05	14.46±0.08	14.35±0.11	AAA	000	--	1.88	
22	10435230-5939222	1.87	13.03±0.04	11.90±0.06	11.20±0.04	AAE	000	--	3.55	Mass-deg.
23	10435408-5941463	1.19	15.40±0.07	14.24±0.05	13.79±0.05	AAA	000	5.47	1.40	
24	10435419-5938073	2.13	13.03±--	13.70±0.06	13.53±0.07	UAA	0cc	--	--	
25	10435501-5936242	0.75	11.64±0.02	11.48±0.03	11.37±0.03	AAA	000	0.42	8.28	
26	10435505-5947505	0.70	14.18±0.03	13.81±0.04	13.70±0.06	AAA	000	--	2.24	
27	10435545-5942531	0.50	14.93±0.05	14.11±0.05	13.84±0.06	AAA	000	2.37	1.81	
28	10435557-5949226	0.39	13.44±0.03	12.65±0.03	12.24±0.03	AAA	000	5.08	2.45	
29	10435606-5949351	1.97	14.53±0.05	13.83±0.05	13.60±0.06	AAA	000	1.87	2.07	
30	10435684-5942364	0.45	14.70±0.05	13.57±0.03	12.88±0.04	AAA	000	9.63	1.97	K-excess

Column 3 ("Offset") is the offset between X-ray and near-IR counterpart. Ph.Q refers to the 2MASS photometric quality flags for the J, H and, K_s bands: "A" to "D" indicate decreasing quality of the measurements, "U" that the value is an upper limit. The next column refers to the contamination and confusion flag: For further analysis we considered only sources unaffected by known artifacts, i.e. Cont. = 000 (see 2MASS documentation for details). Masses are given in solar units, and the last column contains information presented in § 4. Note: the "MASS-DEG." flag indicates mass degeneracy according to a Siess-based Jmag-Mass calibration.

taken from the MS calibration of Knödlseder (2000) and Bessell & Brett (1989). For later spectral types (masses between 0.1 and 7 M_⊙), we adopted the 3 Myr isochrone from Siess et al. (2000), converted to the observational plane using the calibration given by Kenyon & Hartmann (1995). The adopted MS and 3 Myr isochrone overlap satisfactorily.

In order to estimate the typical visual absorption of cluster members, we computed the distance of each X-ray source from the cluster locus along the reddening direction on the K_s vs J-H plane (see Fig. 4-right). Resulting A_v values for individual sources¹⁹ are listed in column 9 of Table 2. Note that for 11.2 < K_s < 12.8 the absorption cannot be constrained because the reddening vector intersects the cluster locus more than once. In both CM diagrams, some X-ray sources, of the order of 20, lie to the left of or relatively close to the unreddened cluster loci. These are likely to be foreground MS stars

and thus their A_v values either cannot be computed or are close to zero. In a statistical sense, the median A_v value of OB stars (A_v = 2.0 ± 0.8 mag.) is lower than that computed for low-mass stars (A_v = 3.6 ± 2.4 mag., considered to be the typical absorption of the cluster). Obviously, the above estimates depend on the reliability of the assumed cluster locus and on the assumption that disk-induced excesses do not significantly affect the J and H magnitudes. To caution of possible contamination and/or anomalous J magnitude, but in particular for the H-band, the median A_v for the low-mass star population was estimated by discarding sources with intrinsic K_s excesses (i.e. labeled with asterisks in figures 3 and 4). We must note that: *i*– the dispersion along the J-K_s axis (see Fig 4-left) indicates differential absorption of the region, and translates in a broad A_v distribution, with a spread 1σ ~2.4 mag. *ii*– the difference between median A_v values of low-mass and OB stars suggests a clearing effect of strong winds and radiation field of massive stars on their surrounding environment. This conclu-

¹⁹ Individual photometric errors of up to 0.1 mag at K_s and J-H color errors of ~0.14, could result in A_v errors up to ~0.7 mag.

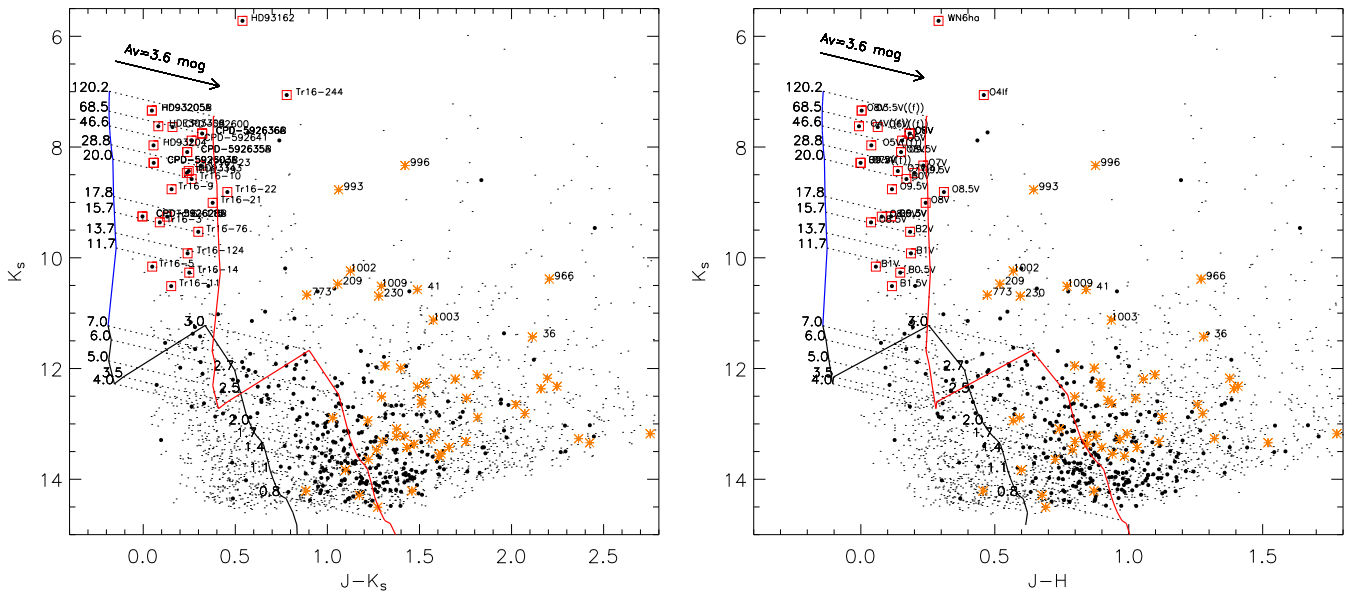


Fig. 4. CM diagrams of the Trumpler 16 region. Symbols as in figure 4. The two parallel curves indicate the expected cluster loci for the assumed distance and no reddening, and for the mean reddening $A_v = 3.6$ mag. Masses are indicated on the left side of the unreddened isochrone. Identified OB stars show K_s magnitudes below 11. Stars with K_s excess show typically $J - K_s > 1$. Note: The limitation imposed by the 2MASS photometry ($K_s \sim 14.5$ mag) corresponds to a mass limit of $1.1 M_\odot$. Labels near OB stars refer to *Simbad names* (left) and respective *Spectral types* (right). The fact that stars Tr16-244 (O4If) and HD93129AB (WN6ha+O4f) appear above the $120 M_\odot$ track does not mean that they are more massive, since their evolutionary stages cannot be compared with a MS isochrone. η Carinae was discarded because of the bad 2MASS photometry (Phot.qual.=’DDD’, see text). Sources labeled with numbers indicate stars (with masses above $12 M_\odot$) probably surrounded by disks.

sion was also reached by Albacete Colombo et al. (2007) for massive stars of the Cyg OB2 region. However, compared to the Cyg OB2 region, the fraction of disk-stars members in the Trumpler 16 region is about four times larger.

Finally, we use the 2MASS J-band magnitudes to obtain an estimate of stellar masses for 510 counterparts (of a total 660 identified stars) with J-band *Phot.Qual.* = 'A' to 'D'. We compute the mass vs. J mag relationship appropriate for the cluster mean age (3 Myr), distance (DM=11.78 mag) and extinction ($A_v = 3.6$ mag), this latter obtained as described above for the cluster locus in the CM diagrams²⁰. We use Siess et al. (2000) models to compute PMS tracks of low- and intermediate-mass stars (masses $\leq 7 M_\odot$). We interpolated the J mag - mass relation, using the J magnitude vs. mass relationship at 3 Myr (see column 10 of Table 2), to compute individual masses of stars²¹. Unfortunately, the relation mass-J mag degenerates in the mass ranges 0.2 - $0.65 M_\odot$ (3 sources) and 2.7 - $4.52 M_\odot$ (21 sources). We indicate these sources with "Mass-deg." flag in column 11 of Table 2, and give mean mass values for sources lying in these two ranges, i.e. 0.42 and 3.55, respectively. Computed masses

over $7 M_{\odot}$ are potentially affected by large uncertainties in the extrapolated J mag - mass relation, and these values were excluded from further analysis. In Table 2 we give masses for a total of 510 stars, of which 410 range between 0.65 and $2.52 M_{\odot}$.

5. X-ray variability

PMS stars have high levels of X-ray activity that are commonly attributed to a "scaled up" solar-like corona formed by active regions. X-ray variability over a wide range of time scales is common in all magnetically active stars (e.g. Feigelson & Montmerle, 1999; Favata & Micela, 2003; Güdel, 2004). On long time scales, this includes rotational modulation of active regions, their emergence and evolution and magnetic cycles (e.g. Marino et al., 2003; Flaccomio et al., 2005). Most of the observed variations have short time-scales (\sim hours), however, and can be attributed to small scale flares triggered by magnetic reconnection events.

We first investigated X-ray variability in our sources using the non-binned one-sample Kolmogorov-Smirnov (KS) test (Press et al., 1992). This test compares the distribution of photon arrival times with that expected for a constant source. The test was applied to photons in the source extraction regions, which also contain background photons. Given that the background was found to be constant with time (§2.1), the results, i.e. the confidence with which we can reject the hypothesis that the flux was constant during our observation, can be attributed to the source photons. Table 1, column 18, reports the logarithm

²⁰ The choice of the J band is justified because (i) in the presence of disk excesses the J-band is the most representative of the photospheric emission i.e. least affected and (ii) the mass ranges in which the mass-luminosity relationship is degenerate are narrower than for a similar relationship in the H and K_s bands.

²¹ This method suffers of photometry inaccuracy, distance and age spread. Mass values should be adopted carefully and should not be considered to measure the slope of the mass function.

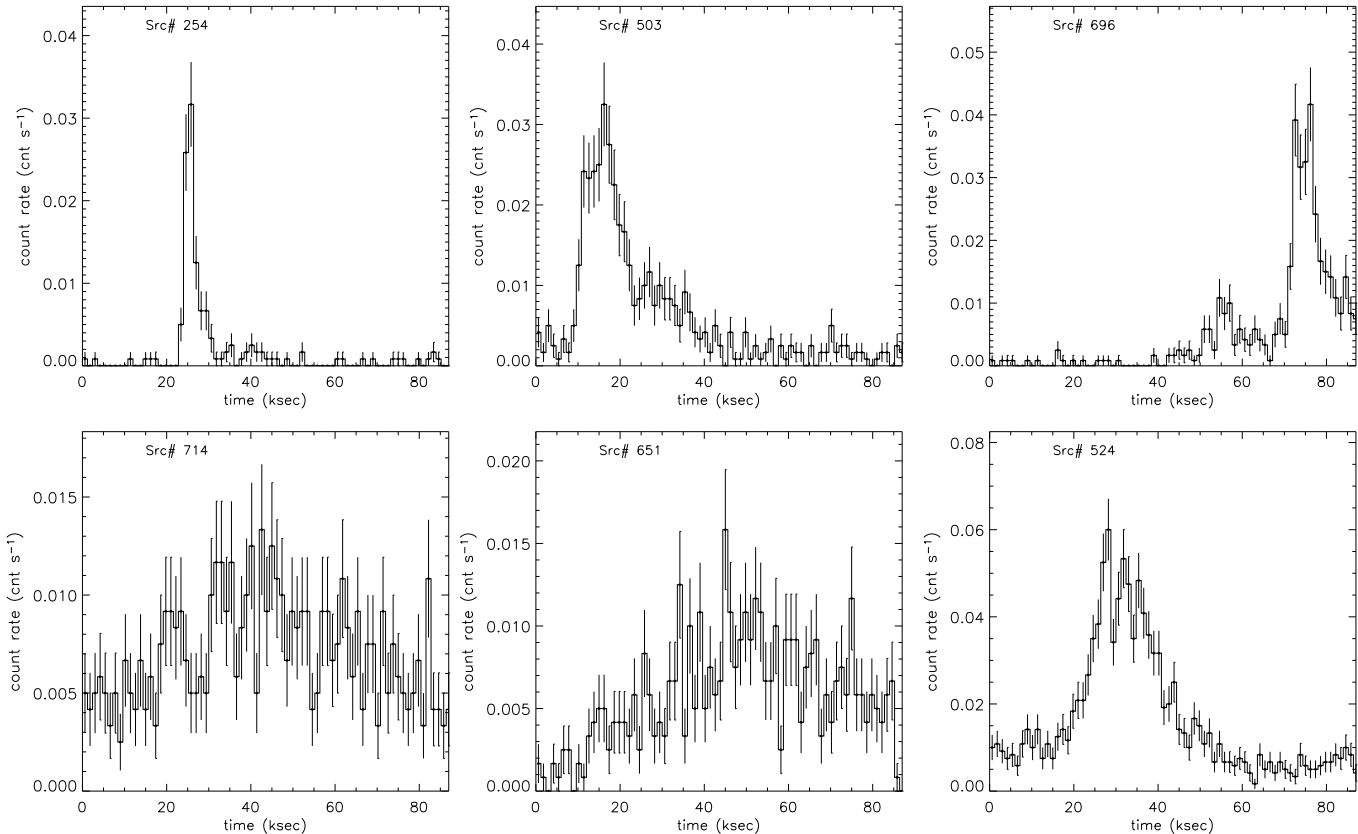


Fig. 5. Light curves (in the 0.5–8.0 keV band) showing different variability scenarios occurring among our 77 variable sources. Bin size is 900 sec. The source number is indicated in each panel. Upper panels show a flare-like behavior with very quick rises and decay phases of hours, while bottom panels are slowly modulated variability. A probable flare+modulation variability is occurring in the last panel.

of the KS-test significance with values <-4 truncated at that value: sources with $\log(P_{KS}) < -3.0$ can be considered almost definitely variable as we expect at most one of the 1035 sources (i.e. $\leq 0.1\%$) to be erroneously classified as variable. Seventy-seven X-ray sources ($\approx 7.4\%$ of the total) fall in this category. Fifty-five sources with $-2.0 < \log(P_{KS}) < -3.0$ can be considered as likely variable, although about half of them suffers of low photon statistics. These numbers of sources are lower limits to the total number of variable sources in the region for several reasons: i) most of the observed variability is in the form of flares, i.e. events that are shorter than our observation and with a duty-cycle that may be considerably longer (Wolk et al., 2005); ii) the sensitivity of statistical tests to time variability of a given relative amplitude depends critically on photon statistics (see Albacete Colombo et al. (2007)). Hereafter, we consider variable those 77 sources with $\log(P_{KS}) < -3$.

To get a more accurate description of the detected variability, we extracted binned light-curves for each of the 77 variable sources in the region. We adopt a bin length of 900 seconds, a compromise between bins that are long enough to reach a good signal-to-noise ratio per bin for most sources and sufficiently short to resolve the decay phase of typical flares. Since the background of our observation is both low (negligible for many sources) and constant in time, we did not apply any background subtraction to the presented light-curves.

In Fig 5 we show examples of the different behavior among the light-curves of variable sources. Source #254 like others (#35, #270, #438, #468, #480, #596, #761 and #975) experience “impulsive” flares with very quick rises and decay phases of only a few hours. Others (sources #503 (#36, #41, #136, #164, #260, #489, #523, #731 and #811) show longer (2 to 10 hours) flares. In several instances a second impulsive event is visible during the exponential decay of a previous flare (e.g. sources #36, #52, #87, #196, #564, #600, #620 and #623). The case of source #696 is a combination of both variability types, with two consecutive flares. Other sources like #714 and #651 (e.g. #27, #251, #271, #793, #839, #890, #904 and #980) show light-curves that, instead of showing typical flares, are characterized by slow continuous rises or decays that might be explained by rotational modulation of non-homogeneously distributed plasma (Flaccomio et al., 2005). Finally, light-curves, like those observed for sources #524, #71 and #933, seem to be related to a combination of flare like activity and rotational modulation.

5.1. Variability in massive stars

Because X-ray emission from O stars, which is believed to be unrelated to solar-like magnetic activity, comes from the integrated emission from a large number of small shocks

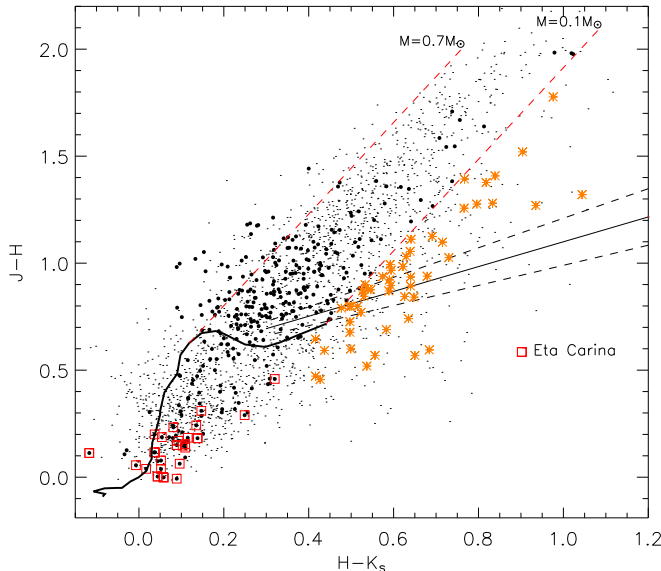


Fig. 3. JHK_s color-color diagram from high quality 2MASS photometry. FILLED CIRCLES and dots refer to X-ray detected and undetected 2MASS sources, respectively. ASTERISKS show the source population with intrinsic K_s excess. Identified 2MASS source known as O- and early B-type stars are indicated by SQUARES. The main sequence is shown for reference. We also show the CTTS locus of Meyer et al. (1997) and reddening vectors (*dashed lines*) with length corresponding to A_v = 13 mag. Note: *i*– the 2MASS photometry of η Carinae is severely affected, with Phot.Qual.=’DDD’; *ii*– the peculiar position of the red box with H-K_s <-0.1 corresponds to the massive binary CPD-592628AB (SpT: O9.5V+B0.3V).

randomly occurring in their strong winds (Feldmeier et al., 1997; Owocki & Cohen, 1999), on average, global X-ray variability is not expected to occur. However, it is surprising that three (out of 28) massive stars, namely Tr 16-11 (B1.5 V, source #136), Tr 16-5 (B1 V, source #489) and the binary HD 93205 (O3.5V((f))+O8V, source #242), are significantly variable, with log(P_{KS}) values lower than -3. The origin of the observed flare-like variability in the first two sources (B-type stars) is probably coronal activity of unresolved late-type companions. This hypothesis was also proposed for Tr16-11 itself by Evans et al. (2003).

Fig 6 shows the X-ray light-curve of the HD 93205 binary system. Two different processes may be acting simultaneously to explain the observed variability:

- i*– The decrement of count rate agrees with phase-locked X-ray variability reported by Morrell et al. (2001). The X-ray count rate decreases from ~ 0.055 to 0.033 cts/s (about 35%) in about 88 ksec (~1 day) of continuous observation, i.e. about 16% of the orbital period. This is in agreement with X-ray emission from colliding winds contributing most of the total detected emission. However, we cannot discard that magnetically channelled wind streams, at the O3.5 V((f)) primary, collide with the cool and dense postshock plasma at the magnetic equator (e.g. θ Orionis-C, Gagné et al., 2005a). A detailed spectral and time (phase-

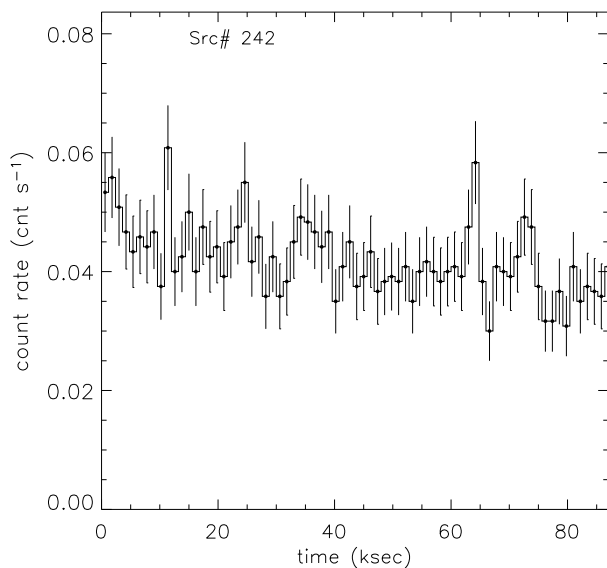


Fig. 6. X-ray light-curve of the massive binary (O3.5V((f))+O8V) HD 93205. This light-curve shows: *i*– a uniform decay probably related to the orbital motion of the system, with changing absorption N_H of the colliding-wind region along the line of sight, plus *ii*– a probable short-term variability (see text).

resolved) study should be follow to discern between these two possibilities.

- ii*– The observed short time X-ray variability (log(P_{KS}) = -3.07). While dynamical instabilities (Luo et al., 1990)²² in the Colliding Wind Region (CWR) seems to be more appropriate, the magnetic reconnection from an unknown low-mass tertiary companion²³ cannot be rule out.

We remark that the origin of X-ray variability in high mass stars is out of the scope of this work, it needs for a large X-ray data-set. We leave this subject to a further investigation.

6. Spectral analysis

In order to characterize the hot plasma responsible for the X-ray emission of Trumpler 16 stars, and to estimate their intrinsic X-ray luminosities, we analyzed the ACIS spectra of the 615 (out of all 1035) sources with more than 20 net photons (NET_CNTS), i.e. corrected for local background. Spectral parameters for sources with less than 20 net photons are too much ill-constrained (Albacete Colombo et al., 2007), and thus were not determined. Moreover, high local background could

²² Whenever the wind velocities of two stars are not equal, shocked CWR should be subject to the rapid growth of dynamical (Kelvin-Helmholtz) instabilities, reaching the radiative cooling state. This limit becomes important for massive binaries with typical orbital periods ≤ 20 days (Antokhin et al., 2004)

²³ Variability like HD 93205’s has been seen also on theta 2 Ori-A and has been interpreted by Schulz et al. (2006) as evidence of binary-induced reconnection. However, Image reconstruction shows that hard, short-term variations are from an intermediate-mass tertiary companion at ~ 0.3 arcsec (Harvin et al., 2002).

affect the reliability of computed spectral parameters. We define the fraction f_{cont} as the ratio between BKG_CNTS (number of background counts in the source extraction region) and NET_CNTS. We accepted spectral fits for sources with $f_{\text{cont}} < 1$ and $\text{NET_CNTS} \geq 20$ photons. Of all 1035 sources, only 563 satisfy both conditions above, while 119 show $f_{\text{cont}} < 1$ and 353 lie in the low statistics regime (i.e. $\text{NET_CNTS} < 20$ ph).

Source and background spectra in the 0.5-8.0 keV band were produced with AE (see §3.2), along with individual “redistribution matrices files” (RMF) and “ancillary response files” (ARF). For model fitting, spectra were grouped so to have a specified number of events in each energy bin. Grouping was tuned to the source statistics and we chose 2, 5, 7, 10, and 60 counts per channel for sources with net-counts in the following ranges: [20-40], [40-100], [100-200], [200-500], and [500-**]. Spectral fitting of background-subtracted spectra was performed with XSPEC v12.0 (Arnaud, 2004) and our own shell and TCL scripts to automate the process as described in Flaccomio et al. (2006). Because background corrected spectra are not appropriately handled by C-statistics (Getman et al., 2005), best-fit parameters for the chosen models were computed by means of the Chi-Squared (χ^2) minimization.

We fit our spectra assuming emission by a thermal plasma, in collisional ionization equilibrium, as modeled by the APEC code (Smith et al., 2001). Elemental abundances are not easily constrained with low-statistics spectra and were fixed at $Z=0.3 Z_\odot$, with solar abundance ratios taken from Anders & Grevesse (1989). The choice of sub-solar abundances is suggested by several X-ray studies of star forming regions (e.g. Feigelson et al., 2002; Preibisch, 2003). Absorption was accounted for using the WABS model, parameterized by the hydrogen column density, N_H (Morrison & McCammon, 1983a). In Table 3 we give best-fit parameters (χ^2_ν , N_H , kT and L_x) of the sources.

Except for 28 massive O- and early B-type stars, we fit source spectra with one-temperature (1T) plasma models using an automated procedure. In order to reduce the risk of finding a local minimum in the χ^2 spaces, our procedure chooses the best fit among several obtained starting from a grid of initial values of the model parameters: $\log(N_H) = 21.0, 21.7, 22.0, 22.4, 22.7$ and 23.0 cm^{-2} and $kT = 0.5, 0.75, 1.0, 2.0, 5.0 \text{ keV}$. best-fit values of $\log(N_H) < 20.3 \text{ cm}^{-2}$ were truncated at 20.3 for two cases (sources #150 and #944) because, in the 0.5-8.0 keV energy range, ACIS spectra are insensitive to lower column densities. In a similar way, above 10 keV *Chandra* is not able to discriminate between such high temperatures. Therefore, 74 best-fit values of kT above 8 keV were truncated to that value. They are indicated with a flag HARD-TAIL in Table 3.

Fig. 7 shows the distribution of best-fit $\log(N_H)$ values for the 563 fitted sources. They appear to be normally distributed with a median $\log N_H \sim 21.73$ ($N_H = 5.37 \times 10^{21} \text{ cm}^{-2}$) and a FWHM of ~ 0.4 dex. The log-normal distribution of the sources is indicated with the Gaussian curve²⁴. The computed median of N_H ($\sim 5.37 \times 10^{21} \text{ cm}^{-2}$) is converted to a median $A_v = 3.35$ by use of the Vuong et al. (2003) relation: $N_H/A_v = 1.6 \times 10^{21}$

²⁴ Seven sources (#150, #305, #342, #388, #692, #868 and #944) appear to have N_H below 10^{21} cm^{-2} , and are likely foreground stars.

Table 3. X-ray spectral fits of Trumpler 16 sources. The complete version is available in the electronic edition of A&A.

N_x #	Cnts. (ph)	Stat. (χ^2_ν)	$\log(N_H)$ (cm^{-2})	kT (keV)	$\log(L_x)$ (erg/s)	flag
1	30	--	-----	-----	30.51	no-fit
2	36	--	-----	-----	30.58	no-fit
3	208	0.66	22.01 ± 0.16	2.07 ± 0.56	31.58	fitted
4	55	0.94	21.90 ± 0.31	2.96 ± 2.61	30.50	fitted
5	28	--	-----	-----	30.48	no-fit
6	41	--	-----	-----	30.64	no-fit
7	47	--	-----	-----	31.29	Tr16-19
8	54	--	-----	-----	30.76	no-fit
9	45	--	-----	-----	30.68	no-fit
10	25	--	-----	-----	30.42	no-fit
11	41	--	-----	-----	30.72	no-fit
12	132	1.50	21.23 ± 0.62	2.65 ± 0.94	31.08	fitted
13	89	0.40	21.64 ± 0.14	0.67 ± 0.93	30.83	fitted
14	15	--	-----	-----	30.23	no-fit
15	41	--	-----	-----	30.65	no-fit
16	23	--	-----	-----	30.40	no-fit
17	28	--	-----	-----	30.48	no-fit
18	31	0.80	22.32 ± 0.32	1.36 ± 0.88	31.04	fitted
19	7	--	-----	-----	29.93	no-fit
20	30	--	-----	-----	30.51	no-fit
21	25	1.21	21.97 ± 0.65	0.29 ± 0.18	30.02	fitted
22	176	0.94	21.81 ± 0.22	3.32 ± 1.45	31.46	fitted
23	25	--	-----	-----	30.43	no-fit
24	22	--	-----	-----	30.38	no-fit
25	177	1.87	22.00 ± 0.18	2.17 ± 0.74	31.52	fitted
26	44	0.90	21.70 ± 0.27	1.49 ± 0.54	30.38	fitted
27	51	0.50	22.06 ± 0.32	2.11 ± 1.27	31.03	fitted
28	77	0.47	21.28 ± 0.72	1.49 ± 0.44	30.83	fitted
29	36	--	-----	-----	30.59	no-fit
30	12	--	-----	-----	30.12	no-fit

Notes: last column flag: Sources with no spectral information (NO-FIT) have their X-ray luminosities computed by using an average count-rate to L_x conversion factor (see § 7). "HARD TAIL" flag refers to the need of more components in the spectral models. Spectral fit parameters for OB-type stars are not listed here as they are presented in Table 4.

atoms $\text{cm}^{-2} \text{ mag}^{-1}$. We also test the relation $A_v = 0.56 N_H + 0.23$ [N_H in 10^{21}] (Predehl & Schmitt, 1995), for which the median A_v is 3.23 mag. Both of these values are in good agreement with the median $A_v = 3.6$ mag computed from our near-IR analysis (see § 4.3). The 1σ dispersion of the N_H distribution is 0.4 dex. It is translated into typical A_v range between 1.3 to 6.7 mag. of visual extinction. X-ray sources without near-IR counterparts seem to be distributed towards higher absorption values (median $\log(N_H) \sim 21.9 \text{ cm}^{-2}$) with respect to those with near-IR counterparts. Unfortunately, they generally have poor X-ray photon statistics and consequently a less reliable estimation of their X-ray spectral parameters.

Unlike the N_H distribution, the kT distribution of plasma temperatures is not log-normal. It peaks at ~ 1.6 keV, has a median ~ 1.95 keV and shows an extended hard tail attributed both to variable sources ($\log P_{\text{KS}} < -3$) with harder spectra (median $kT = 3.25$ keV, as expected from coronal heating processes involved in flare-like activity) and to highly absorbed sources

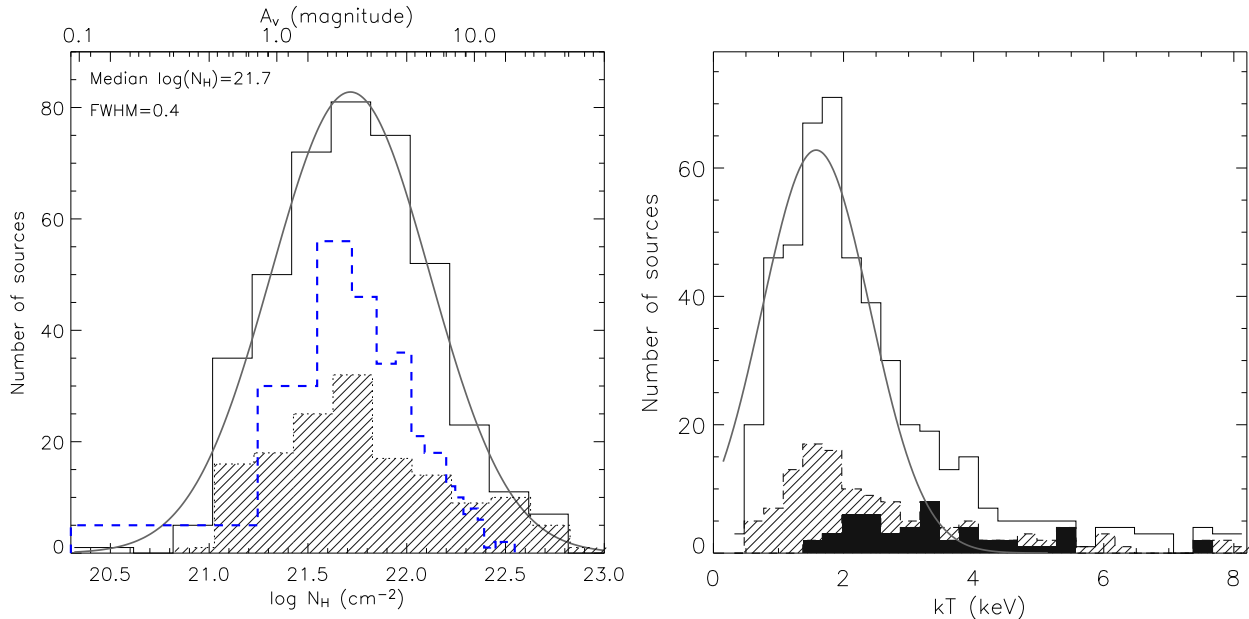


Fig. 7. *Left:* The solid histogram shows the N_H (A_v^{xspec}) distribution of 415 spectral fitted sources with 2MASS counterparts. The upper scale was converted using an N_H/A_v ratio of 1.6×10^{21} . The thick dashed histogram shows the $A_v^{\text{near-IR}}$ mag. distribution for all near-IR counterparts as was computed in § 4. Both distributions peak at $A_v^{\text{xspec}} = 3.35$ ($1\sigma = 0.4$) mag and $A_v^{\text{near-IR}} = 3.26$ mag. ($1\sigma = 0.3$ dex). The shadowed histogram shows the N_H distribution of 148 sources with no near-IR counterpart. *Right:* Same as the *left* panel for plasma temperaturess (kT) with, in addition, the distribution for "flaring" sources (black-filled histogram). The peak of the overal distribution is at ~ 1.6 keV.

(i.e. $A_v \geq 6$ mag) showing a median $kT \sim 2.6$ keV (while those in the range $1 \leq A_v \leq 6$ mag being softer and distributed with a median $kT = 1.75$ keV).

Finally, suspected *single* massive stars show typically soft spectra with median $kT = 0.62$ keV, while for known massive binaries this value rises to $kT = 2.1$ keV, no doubt due to hard X-ray photons being produced in the colliding wind region (CWR) of the massive O+OB binaries. Details of X-ray spectral characteristics of massive stars in the region are presented in § 8.

7. X-ray luminosity of stars

Unabsorbed X-ray luminosities were computed for those sources with available spectral fits, for the [0.5-8.0] keV energy range. For sources with no available and/or reliable spectral fit (119+353 out of 1035) L_x were computed using a single count-rate to L_x conversion factor (CF)²⁵. CF in Trumpler 16 is $8.3_{-5.2}^{+10.3} \times 10^{33}$ ergs/ph. Upper and lower values correspond to $\pm 1\sigma$ uncertainties, respectively.

In Figure 8 we show the X-ray luminosity distribution for low-mass²⁶ stars, while known OB stars are plotted separately in the upper inset histogram. The L_x distribution of sources

²⁵ It was computed as the median ratio between the individual unabsorbed X-ray luminosities (from best-fit spectral models) and the source count-rates.

²⁶ We defined the low mass range $M < 7 M_\odot$, based on the presence of a significant convection envelope (at the adopted age) that explains X-ray emission from magnetic activity.

has been plotted separately for: *i*– 592 X-ray sources with near-IR counterpart, not including 28 OB stars and variable sources (thin solid histogram), with a median $\log(L_x) \sim 30.5$ erg s⁻¹. The peak of the distribution marks indeed the completeness limit of our X-ray observation; *ii*– 354 unidentified sources, except for variable ones, which appear systematically less luminous than those with 2MASS counterpart, with median $\log(L_x) \sim 30.2$ erg s⁻¹; *iii*– 77 variable sources, showing a median $\log(L_x) \sim 31.1$ erg s⁻¹, i.e. about 4 times higher than the observed L_x for similar stars in a quiescent (non-flaring) phase. The upper inset in Fig 8 shows the unabsorbed L_x for 28 massive stars (including 13 binary systems) in the region. By following results and discussion presented in § 8, binaries appears with typical L_x over 10^{32} erg s⁻¹, higher than observed for those suspected single B-type stars. As we will discuss in § 8, massive binaries have typical X-ray luminosities $L_x \geq 10^{32}$ erg s⁻¹, higher than those of single OB stars.

We examine how X-ray activity depends on stellar mass for Trumpler 16 low-mass stars, and compare the results with those already known for the ONC and Cyg OB2 SFRs. In order to increase statistics, we use L_x values computed by means of the average CF. While L_x and mass for Cyg OB2 stars were computed following the same procedures used here (Albacete Colombo et al., 2007), for ONC stars they were computed differently in the literature²⁷. For the sake of homogeneity

²⁷ In the ONC, stellar masses were computed from optical spectra, available for many stars, while L_x was obtained for many stars from an X-ray spectral analysis based on a relatively high photon statistics (Getman et al., 2005).

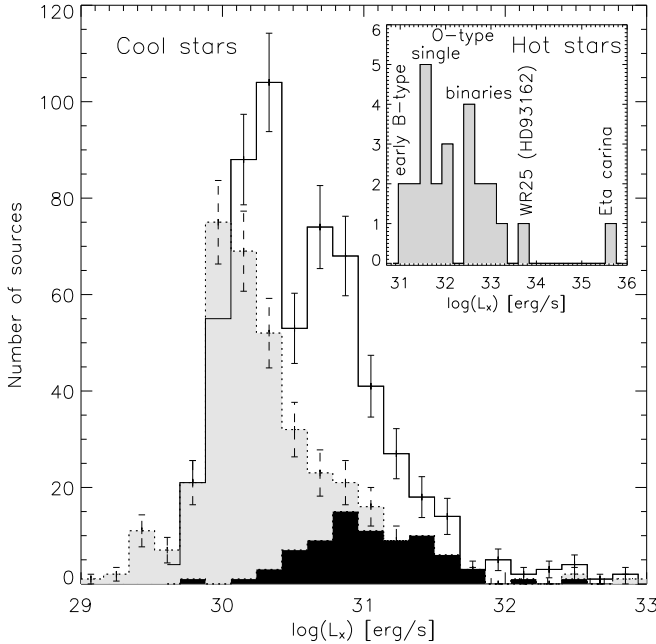


Fig. 8. The X-ray luminosity distribution for 592 low-mass stars computed from a single L_x -Count rate conversion factor is shown as a *solid line*. The *grey filled* histogram shows the L_x distribution for 354 X-ray sources without near-IR counterpart. The 77 variable sources are shown with the *black-filled* histogram. Upper-right inset (Hot stars) shows the unabsorbed L_x from X-ray spectral fits (see § 8). Error bars are 1σ Poisson errors.

ity, we have re-computed L_x and masses of ONC stars by using a single count-rate to L_x conversion factor ($CF_{onc}=7.52\times10^{+32}$ erg/ph) and 2MASS photometry, respectively.

In Figure 9 we show a plot of L_x vs. star mass. We use circles for all 510 Tr16 sources with estimated masses. Filled (329) and open (181) circles indicate L_x values computed from spectral fits and using the CF, respectively. We perform a linear regression for all sources in the $0.7-2.5 M_\odot$ range: $\log(L_x)=30.26(\pm0.11)+1.0(\pm0.09)\log(M/M_\odot)$ with a standard deviation in the residuals of 0.38 dex. The power-law slope we find here is in agreement with that found by Albacete Colombo et al. (2007) for the Cyg OB2 region: $\log(L_x)=30.33(\pm0.16)+0.71(\pm0.13)\log(M/M_\odot)$ for masses in the $0.5-3.0 M_\odot$ range. This slope also agrees with that we find for the ONC stars in the mass range $0.5-3.0 M_\odot$, namely 0.82 ± 0.09 .

Changes in the X-ray activity of stars with different ages of the SFRs has been previously reported by Preibisch & Feigelson (2005). To address this issue, we computed L_x detection limits for low-mass stars in the Tr16(3 Myrs), CygOB2(2 Myrs) and ONC(1 Myr) observations, as $\log(L_x) \sim 30.5, 30.3$ and 28.5 erg s $^{-1}$, respectively, above which a source is detectable anywhere in the FOV. A mass-dependent completeness fraction (f_{comp}) for our survey of Trumpler 16 stars was then computed by adopting the X-ray Luminosity Functions given by Preibisch & Feigelson (2005): f_{comp} is $\sim 5\%$ for $0.1-0.5 M_\odot$, $\sim 40\%$ for $0.5-0.9 M_\odot$ and

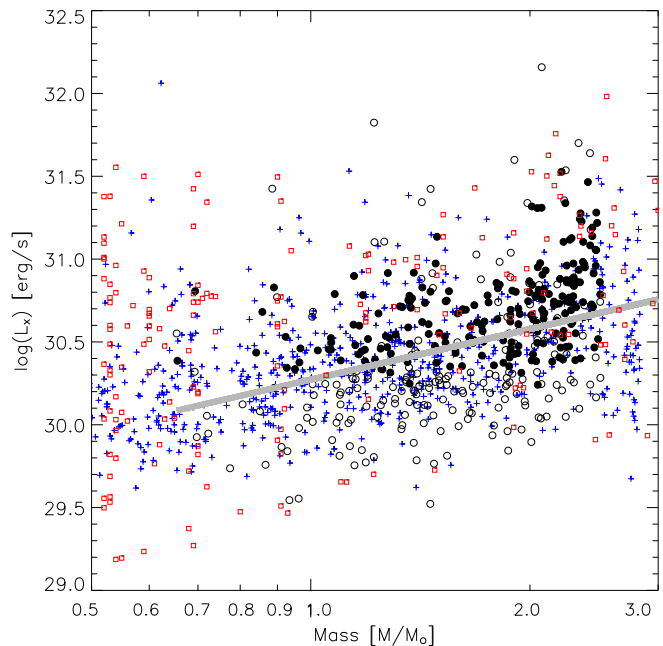


Fig. 9. X-ray luminosity vs. stellar mass for stars in the near-IR sample with masses determined from the PMS models of Siess et al. (2000). Tr16 stars are plotted by open and filled circles, corresponding to L_x from CF and spectral fits, respectively. Crosses indicate Cyg OB2 sources (Albacete Colombo et al., 2007), while small boxes are ONC sources (Preibisch et al., 2005). The thick gray line shows the linear regression fit to the Tr16 low-mass ($0.7-2.5 M_\odot$) stars.

$\sim 55\%$ in the $0.9-1.2 M_\odot$ range. Our survey of Tr 16 is statistically complete for masses $\geq 1.5 M_\odot$. In Figure 10 we present L_x cumulative distributions for Trumpler 16, Cyg OB2 and ONC stars in the mass range $1.5-2.5 M_\odot$ where all three data sets are complete. While Trumpler 16 and Cyg OB2 show very similar distributions, the ONC looks quite different with respect to Tr16. The distance between two distributions ($D=0.31$) was computed using a two-sample Kolmogorov-Smirnov test (Press et al., 1992). We are able to confirm, with a probability $\geq 99.9\%$ ($\log(P_{ks})=-4.15$), that young ONC (1 Myr) stars, with masses in the range $1.5-2.5 M_\odot$, are intrinsically more luminous in X-rays than their Tr16 (3 Myr) counterparts.

8. X-rays from massive stars

A variety of different physical mechanisms are responsible for the observed X-ray emission in OB-type stars. The most widely accepted explanation invokes multiple small-scale shocks in the inner layers of their radiation-driven stellar winds (e.g. Feldmeier et al., 1997). In recent years it has gained importance a plasma heating model known as *magnetically channeled wind shock* (MCWS) (Schulz et al., 2003; Owocki et al., 2005; Gagné et al., 2005b). Moreover, WR+OB and/or O+OB *interacting wind binary systems* produce an excess of X-ray emission from the CWR (Stevens et al., 1992; Zhekov & Skinner, 2000; Pittard & Stevens, 2002).

Table 4. Stellar parameters and X-ray spectral results for massive stars.

N _x #	Name	Stellar parameters				X-ray spectral parameters					Notes	
		Spectral Type	L _{bol} [L _⊙]	M [M _⊙ /yr]	L _w [L _⊙]	χ^2_{ν} /d.o.f	N _H [10 ²²] cm ⁻²	Abund. [Z _⊙]	kT ₁ [keV]	kT ₂ [keV]	L _X [erg/s]	
7	Tr16-19	O9.5V	47863	0.150	33.00	1.01/28	0.55±0.25	(1.0)	0.63±0.17	---	1.95 ^{2.2} _{0.9} 10 ³¹	
52	Tr16-124	B1V	23442	0.08	8.800	0.98/28	0.75±0.33	0.18	0.49±0.28	2.27±1.26	4.13 ^{4.2} _{1.4} 10 ³¹	
74	HD93162	WN6ha	1659586	10.5	5140	1.9/240	0.63±0.03	0.54	0.71±0.01	2.66±0.06	5.23 ^{5.32} _{5.17} 10 ³³	fl-6.7 keV
89	Tr16-244	O4If	851138	10.0	7060	0.95/54	1.50±0.11	0.53	0.43±0.06	1.09±0.31	1.01 ^{1.04} _{0.53} 10 ³³	em-lines
136	Tr16-11	B1.5V	19055	0.06	4.400	1.02/17	0.79±0.23	(1.0)	0.42±0.24	3.05±1.48	4.05 ^{5.05} _{1.58} 10 ³¹	variable
207	Tr16-10	B0V	37154	0.120	22.00	0.90/19	0.35±0.31	(1.0)	0.59±0.13	2.85±1.50	1.88 ^{1.93} _{0.96} 10 ³¹	
228	HD93204	O5V((f))	309029	1.30	780.0	1.08/33	0.21±0.07	0.42	0.50±0.06	---	6.15 ^{9.96} _{1.55} 10 ³¹	
242	HD93205A	O3.5V((f))	575440	2.50	1870	2.12/74	0.66±0.04	1.2	0.26±0.02	1.73±0.60	1.89 ^{2.26} _{1.06} 10 ³³	(A),primary,CW
242	HD93205B	O8V	91201	0.260	91.00	"	"	"	"	"	"	(B),secondary,CW
281	Tr16-21	O8V	91201	0.260	91.00	1.09/14	0.66±0.31	(1.9)	0.33±0.18	---	2.92 ^{3.41} _{0.09} 10 ³¹	
286	Tr16-14	B0.5V	29512	0.100	17.00	---	---	---	---	---	---	not fitted
352	CPD-592600	O6V((f))	208929	0.800	410.0	1.07/45	0.54±0.12	1.0	0.29±0.05	0.78±0.11	3.12 ^{3.70} _{1.76} 10 ³²	
407	CPD-592603A	O7V((f))	138038	0.400	170.0	1.08/23	0.58±0.14	(1.0)	0.31±0.07	---	1.29 ^{1.79} _{0.87} 10 ³²	(A),primary
407	CPD-592603B	O9.5V	47863	0.150	33.00	"	"	"	"	"	"	(B),secondary
407	CPD-592603C	B0.2V	37153	0.120	22.00	"	"	"	"	"	"	(C),open
489	Tr16-5	B1V	23442	0.08	8.800	1.13/18	0.23±0.09	(1.0)	2.87±0.88	---	1.26 ^{1.43} _{1.08} 10 ³¹	variable
649	η Carinae -MS	O2If	3715354	8.32	6780	3.75/342	7.39±0.39	4.25	0.27±0.32	7.16±3.6	4.02 ^{8.5} _{0.6} 10 ³⁵	(A),fl-6.7 keV
649	η Carinae -B	O5V	309029	1.30	780.0	"	"	"	"	"	"	(B),CW,variable
687	Tr16-23	O7V	138038	0.400	170.0	0.78/23	0.60±0.09	(1.0)	0.46±0.07	---	5.53 ^{6.51} _{4.34} 10 ³¹	
688	Tr16-9	O9.5V	47863	0.150	33.00	1.02/13	0.48±0.29	(1.0)	0.30±0.16	1.0±0.23	3.78 ^{4.20} _{1.40} 10 ³¹	
689	HDE303308	O4V((f))	467735	2.00	1410	1.80/49	0.54±0.05	(1.0)	0.25±0.03	0.52±0.09	6.16 ^{7.87} _{6.10} 10 ³²	em-lines
707	Tr16-3	O8.5V	72443	0.220	67.00	0.74/16	0.25±0.15	(1.0)	0.33±0.15	---	1.10 ^{1.27} _{0.19} 10 ³¹	
729	CPD-592628A	O9.5V	47862	0.150	33.00	1.08/17	0.93±0.79	(1.0)	0.11±0.17	0.96±0.74	3.11 ^{6.05} _{1.79} 10 ³²	(A) primary
729	CPD-592628B	B0.3V	37153	0.120	22.00	"	"	"	"	"	"	(B) secondary
730	Tr16-22	O8.5V	72443	0.220	67.00	1.3/64	1.07±0.10	(1.9)	0.35±0.07	1.86±0.12	7.71 ^{9.34} _{7.06} 10 ³²	prob. binary
759	Tr16-74	B1V	23442	0.0800	8.800	---	---	---	---	---	---	not fitted
803	HD93343	O7V(n)	138038	0.400	170.0	0.93/32	0.78±0.09	(1.0)	0.28±0.03	>4.0	2.96 ^{3.92} _{2.63} 10 ³²	em-lines
807	Tr16-76	B2V	15488	0.05	2.200	---	---	---	---	---	---	not fitted
808	CPD-592635A	O8V	91201	0.260	91.00	0.88/28	0.58±0.12	(1.0)	0.28±0.03	0.90±0.17	1.40 ^{1.86} _{1.09} 10 ³²	(A),SB2
808	CPD-592635B	O9.5V	47862	0.150	33.00	"	"	"	"	"	"	(B) SB2
812	CPD-592636A	O7V	138038	0.400	170.0	1.05/33	0.74±0.09	(1.0)	0.25±0.04	0.87±0.12	3.56 ^{4.66} _{2.28} 10 ³²	(A),(SB2),em-lines
812	CPD-592636B	O8V	91201	0.260	91.00	"	"	"	"	"	"	(B),SB2
812	CPD-592636C	O9V	58884	0.180	47.00	"	"	"	"	"	"	(C),SB1
854	CPD-592641	O5V	309029	1.30	780.0	0.87/36	0.87±0.08	(1.0)	0.25±0.07	0.56±0.11	5.48 ^{7.63} _{3.55} 10 ³²	em-lines
888	Tr16-115	O8.5V	72443	0.220	67.00	1.01/10	0.54±0.32	(1.0)	0.28±0.18	0.54±0.32	3.06 ^{3.34} _{0.87} 10 ³¹	
997	FO15A	O5.5V((f))	309029	1.30	780.0	0.83/29	1.15±0.15	(1.0)	0.75±0.10	>7.5	1.05 ^{1.31} _{0.82} 10 ³²	(A),SB2,em-lines
997	FO15B	O8.5V	91201	0.260	91.00	"	"	"	"	"	"	(B),SB2

Notes: it "em-lines" refers to stars with emission lines in their optical spectra. "CW" notes those binaries with a colliding wind region. "Open" refers to those long period binaries, i.e. with well-separated components. Components (A), (B), (C) refer to system components sorted according to mass decrease.

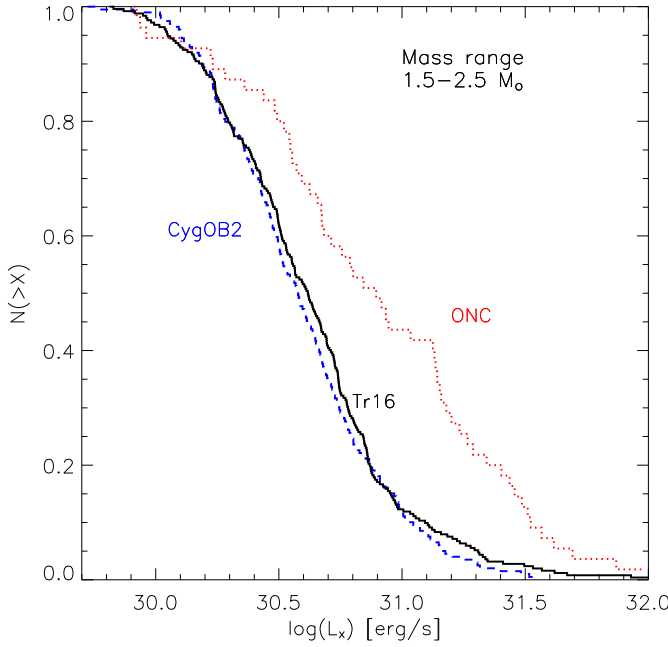


Fig. 10. Cumulative distributions of X-ray luminosities for Trumpler 16 low-mass stars with masses $1.5 \leq M/M_{\odot} \leq 2.5$ (thick solid line). Dotted and dashed lines represent the L_x cumulative distributions for ONC and CygOB2, respectively, in the same mass range.

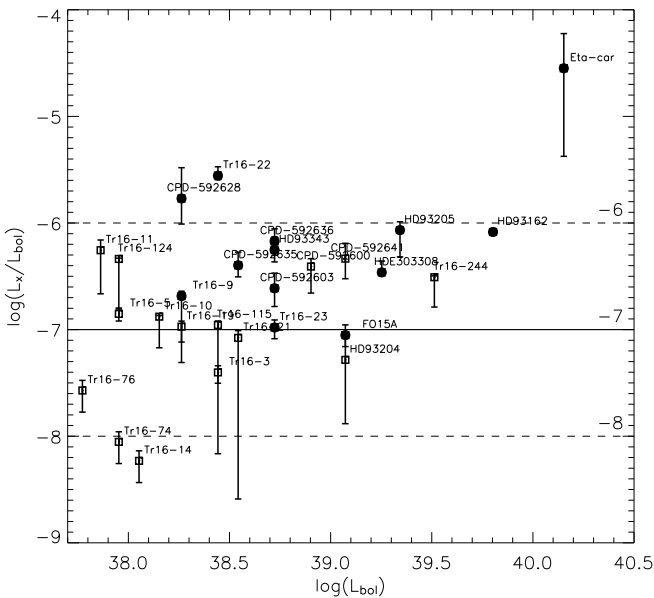


Fig. 11. $\log(L_x/L_{bol})$ versus $\log(L_{bol})$ relation for massive stars in Tr16. Open boxes refer to suspected single stars and filled circles to known binaries. Notes: *i*—Because of flare-like variability (see §5.1) observed in Tr16-#5 (B1.5V) and Tr16-#11 (B1V), their X-ray emission is probably dominated by an unknown low-mass star companion. *ii*—The star Tr16-#22 (O8.5V+?) has the highest $\log(L_x/L_{bol})$ ratio (~ -5.56) among all MS OB-type stars of the region.

Given the relatively large number of massive OB-type stars in the region, it is appropriate to show in Table 4 most relevant

stellar parameters of the massive stars (L_{bol} , \dot{M} , and L_{wind} computed as $\frac{1}{2}\dot{M}v_{\infty}^2$)²⁸. We computed L_x by use of an absorbed (wabs) thermal plasma model (APEC). Metal abundance was fixed at $Z=0.3Z_{\odot}$ in fitting faint sources (< 100 ph.), while it was left as a free parameter for the remaining cases (see Table 4). In Fig 11 we show the L_x/L_{bol} relation. In spite of the observed scatter, one sees that the median L_x/L_{bol} for binaries (filled circles) is about 7 times larger ($\sim 8.3 \times 10^{-7}$) than that of suspected single stars ($\sim 1.1 \times 10^{-7}$)²⁹. Four of the 13 known binaries in the analysis are well separated systems: the LBV η Carinae, a probable long period binary with $P \sim 2026 \pm 2$ days (Damineli et al., 2007), the Wolf-Rayet star WR25 (HD 93162), a 208-days period binary system (Gamen et al., 2006) and HDE 303308, resolved as a binary system with a component separation of about ~ 38 AU projected along the fine guidance sensor (FGS) y-axis³⁰. The stars Tr16#9 (O9.5 V+?) and Tr16#23 (O7 V+?) show photometric variability probably related to a secondary component (Nelan et al., 2004), and thus we consider them also to be binaries.

Besides of the several works (e.g. Seward et al., 1979; Seward & Chlebowksi, 1982; Corcoran et al., 1995; Albacete Colombo et al., 2003; Evans et al., 2003, 2004; Sanchawala et al., 2007) about the origin of the observed X-ray emission on massive stars of this region, this goal is far out of the scope of our paper and not extensively discussed here.

9. Summary and conclusion

We report here results of a deep *Chandra* X-ray observation pointed toward the ~ 3 Myr old star forming region Trumpler 16. Source detection was performed using the PWDetect code, identifying 1035 X-ray sources in the $17' \times 17'$ ACIS-I FOV. Most of these seem to be outside the obscured V-shaped region of dust and gas. Star formation in this part of the masked region has probably been disrupted and/or diminished as the stellar winds are blocked inside the cloud, due to the efficiency of photo-evaporation processes caused by interactions of the nearby hot massive stars with the dense dust and gas structures.

Data extraction was performed using the semi-automated IDL-based ACIS EXTRACT package, which is well suited to the analysis of observations of crowded fields such as ours.

The X-ray source list was cross-identified with optical and near-IR (2MASS) catalogs: 28 X-ray sources (of 44 within the FOV) were identified with optically characterized OB members of Trumpler 16 and 760 with 2MASS sources. Among these latter sources almost all are believed to be Trumpler 16 members. About 90 X-ray sources without optical/NIR counterparts are

²⁸ Adopted values were taken from Smith (2006)-(table 1)

²⁹ Because of observed flare-like variability in Tr16-#5 and #11, we suspect that most of X-rays emission comes from a low-mass companion, and therefore we discard these sources in computing the median L_x .

³⁰ It was unresolved along the FGS x-axis down to 20 AU, suggesting an eccentric orbit.

estimated to be of extragalactic nature (AGNs), while the remaining X-ray sources with no counterpart are likely associated with members that are fainter than the 2MASS completeness limit.

In order to characterize the previously unidentified likely cluster members with NIR counterparts, we placed them on NIR color-magnitude (K_s vs. $H-K_s$) and color-color ($H-K_s$ vs. $J-H$) diagrams. A first estimate of interstellar extinction was obtained adopting a 3 Myr isochrone for the low- and intermediate-mass stars and assuming that O- and early B-type stars lie on the MS. We find a median visual absorption for OB stars of $A_v \sim 2.0$ mag, while low mass likely members seem to be slightly more absorbed, $A_v \sim 3.6$ mag. We also use the 3 Myr isochrone and the J magnitude to estimate masses of likely members assuming that they share the same distance and absorption. Our sample of X-ray selected members with near-IR counterparts reaches down to $M=0.5-0.6 M_\odot$, and is likely complete down to $\sim 1.5 M_\odot$. From the $H-K_s$ vs. $J-H$ diagram we estimate that $\sim 15\%$ (51/339) of low-mass stars have NIR excesses, finding it to be quite a high percentage with respect to the 2 Myr old Cyg OB2. We believe that the disk fraction in young SFRs is more dependent on spatial morphology of gas and dust around massive stars, which may enhance photo-evaporation, and thus shorten disk lifetimes, than on the total number of massive stars in the region.

At least 77 sources, i.e. $\sim 7.4\%$, were found to be variable within our observation with a confidence level greater than 99.9%. Only three of the 28 detected O- and early B-type stars were detected as variable during our 90-ksec observation, in spite of the high statistics of the OB stars' light curves. These exceptions are the known binary O3.5V+O8V star HD93205 (our source #242), showing a rather linear decay of the count rate during the observation plus a short-term variability, the B1.5 V star Tr16-11 (source #136) and the B1V star Tr16-5 (source#489). The latter two show a flare-like variability probably related to unresolved low-mass companions.

We modeled the ACIS X-ray spectra of sources with more than 20 photons and where $f_{\text{cont}} < 1$. We assumed an absorbed single-component thermal emission model. The median $\log(N_H)$ of the sources is $21.73 (\text{cm}^{-2})$. This value agrees well with the median A_v computed from the near-IR diagram. The median kT of low-mass stars is 2.6 keV. Sources associated with O- and early B-type stars are instead quite soft (median kT : 0.60 keV). Absorption corrected X-ray luminosities of OB stars were calculated from the best-fit spectral models. O and B-type stars are the most luminous, with $L_x = 2.5 \times 10^{30} - 6.3 \times 10^{33} \text{ erg s}^{-1}$. Their X-ray and bolometric luminosities are in rough agreement with the relation $L_x/L_{\text{bol}} = 10^{-7}$, albeit with an order of magnitude dispersion. Low mass stars have L_x ranging between 10^{30} and $10^{31} \text{ erg s}^{-1}$ (median $L_x = 2.8 \times 10^{30}$). Variable low mass stars are on average 0.5 dex brighter ($\log(L_x) \sim 31.0 \text{ erg s}^{-1}$). These X-ray luminosities are consistent with those of similar mass stars in the slightly younger (2 Myr) Cyg OB2 region. However, in the mass range 1.5-2.5 M_\odot , the ONC(1 Myr) shows higher X-ray activity level than observed in Trumpler 16 stars in the same mass range. We believe that the age- L_x activity connection is an acceptable explanation of this result.

Acknowledgements. We thank the referee, Marc Gagne, for his time and many useful comments that improved this work. This publication makes use of data products from the Two Micron All Sky Survey, which is a joint project of the University of Massachusetts and the Infrared Processing and Analysis Center/California Institute of Technology, funded by the National Aeronautics and Space Administration and the National Science Foundation. J.F.A.C acknowledges support by the Marie Curie Fellowship Contract No. MTKD-CT-2004-002769 of the project "*The Influence of Stellar High Energy Radiation on Planetary Atmospheres*", and the host institution INAF - Osservatorio Astronomico di Palermo (OAPA). J.F.A.C is a researcher member of the Consejo Nacional de Investigaciones Científicas y Tecnológicas (CONICET)-Argentina and acknowledges support from this institution. G.M., F.D. and S.S. acknowledge financial support from the Ministero dell'Università e della Ricerca research grants, and ASI/INAF Contract I/023/05/0.

References

- Albacete Colombo, J. F., Flaccomio, E., Micela, G., Sciortino, S., & Damiani, F.: 2007, *A&A* **464**, 211
- Albacete Colombo, J. F., Méndez, M., & Morrell, N. I.: 2003, *MNRAS* **346**, 704
- Alexander, D. M., Bauer, F. E., Brandt, W. N., Schneider, D. P., Hornschemeier, A. E., Vignali, C., Barger, A. J., Broos, P. S., Cowie, L. L., Garmire, G. P., Townsley, L. K., Bautz, M. W., Chartas, G., & Sargent, W. L. W.: 2003, *AJ* **126**, 539
- Anders, E. & Grevesse, N.: 1989, *Geochim. Cosmochim. Acta* **53**, 197
- Antokhin, I. I., Owocki, S. P., & Brown, J. C.: 2004, *ApJ* **611**, 434
- Arnaud, K.: 2004, *AAS/High Energy Astrophysics Division* **8**,
- Barger, A. J., Cowie, L. L., Capak, P., Alexander, D. M., Bauer, F. E., Fernandez, E., Brandt, W. N., Garmire, G. P., & Hornschemeier, A. E.: 2003, *AJ* **126**, 632
- Bessell, M. S. & Brett, J. M.: 1989, *LNP Vol. 341: Infrared Extinction and Standardization* **341**, 61
- Brooks, K. J., Storey, J. W. V., & Whiteoak, J. B.: 2001, *MNRAS* **327**, 46
- Brooks, K. J., Whiteoak, J. B., & Storey, J. W. V.: 1998, *Publications of the Astronomical Society of Australia* **15**, 202
- Broos, P., Townsley, L., Getman, K., & Bauer, F.: 2002, *ACIS Extract, An ACIS Point Source Extraction Package*, <http://www.astro.psu.edu/xray/docs/TARA/>
- Carraro, G., Romanillo, M., Ventura, P., & Patat, F.: 2004, *A&A* **418**, 525
- Corcoran, M. F., Swank, J., Rawley, G., Petre, R., Schmitt, J., & Day, C.: 1995, in V. Niemela, N. Morrell, & A. Feinstein (eds.), *Revista Mexicana de Astronomía y Astrofísica Conference Series*, Vol. 2 of *Revista Mexicana de Astronomía y Astrofísica Conference Series*, pp 97–+
- Damiani, F., Maggio, A., Micela, G., & Sciortino, S.: 1997a, *ApJ* **483**, 350
- Damiani, F., Maggio, A., Micela, G., & Sciortino, S.: 1997b, *ApJ* **483**, 370
- Davidson, K. & Humphreys, R. M.: 1997, *ARA&A* **35**, 1
- DeGioia-Eastwood, K., Throop, H., Walker, G., & Cudworth, K. M.: 2001, *ApJ* **549**, 578

- Evans, N. R., Schlegel, E. M., Waldron, W. L., Seward, F. D., Krauss, M. I., Nichols, J., & Wolk, S. J.: 2004, *ApJ* **612**, 1065
- Evans, N. R., Seward, F. D., Krauss, M. I., Isobe, T., Nichols, J., Schlegel, E. M., & Wolk, S. J.: 2003, *ApJ* **589**, 509
- Favata, F. & Micela, G.: 2003, *Space Science Reviews* **108**, 577
- Feigelson, E. D., Broos, P., Gaffney, III, J. A., Garmire, G., Hillenbrand, L. A., Pravdo, S. H., Townsley, L., & Tsuboi, Y.: 2002, *ApJ* **574**, 258
- Feigelson, E. D. & Montmerle, T.: 1999, *ARA&A* **37**, 363
- Feinstein, A.: 1995, in V. Niemela, N. Morrell, & A. Feinstein (eds.), *Revista Mexicana de Astronomia y Astrofisica Conference Series*, Vol. 2 of *Revista Mexicana de Astronomia y Astrofisica Conference Series*, pp 57–+
- Feldmeier, A., Puls, J., & Pauldrach, A. W. A.: 1997, *A&A* **322**, 878
- Flaccomio, E., Micela, G., & Sciortino, S.: 2006, *A&A* **455**, 903
- Flaccomio, E., Micela, G., Sciortino, S., Feigelson, E. D., Herbst, W., Favata, F., Harnden, Jr., F. R., & Vrtilek, S. D.: 2005, *ApJS* **160**, 450
- Gagné, M., Oksala, M. E., Cohen, D. H., Tonnesen, S. K., ud-Doula, A., Owocki, S. P., Townsend, R. H. D., & MacFarlane, J. J.: 2005a, *ApJ* **628**, 986
- Gagné, M., Oksala, M. E., Cohen, D. H., Tonnesen, S. K., ud-Doula, A., Owocki, S. P., Townsend, R. H. D., & MacFarlane, J. J.: 2005b, *ApJ* **634**, 712
- Gamen, R., Gosset, E., Morrell, N., Niemela, V., Sana, H., Nazé, Y., Rauw, G., Barbá, R., & Solivella, G.: 2006, *A&A* **460**, 777
- Getman, K. V., Flaccomio, E., Broos, P. S., Grossi, N., Tsujimoto, M., Townsley, L., Garmire, G. P., Kastner, J., Li, J., Harnden, F. R., Wolk, S., Murray, S. S., Lada, C. J., Muench, A. A., McCaughrean, M. J., Meeus, G., Damiani, F., Micela, G., Sciortino, S., Bally, J., Hillenbrand, L. A., Herbst, W., Preibisch, T., & Feigelson, E. D.: 2005, *ApJS* **160**, 319
- Giacconi, R., Bergeron, J., Borgani, S., Gilmozzi, R., Hasinger, G., Nonino, M., Norman, C., Rosati, P., Tozzi, P., & Zheng, W.: 2001, *Memorie della Societa Astronomica Italiana* **72**, 831
- Grabelsky, D. A., Cohen, R. S., Bronfman, L., & Thaddeus, P.: 1988, *ApJ* **331**, 181
- Güdel, M.: 2004, *A&A Rev.* **12**, 71
- Hägele, G. F., Albacete Colombo, J. F., Barbá, R. H., & Bosch, G. L.: 2004, *MNRAS* **355**, 1237
- Hanson, M. M.: 2003, *ApJ* **597**, 957
- Harvin, J. A., Gies, D. R., Bagnuolo, Jr., W. G., Penny, L. R., & Thaller, M. L.: 2002, *ApJ* **565**, 1216
- Hofner, P. & Churchwell, E.: 1997, *ApJ* **486**, L39+
- Hofner, P., Delgado, H., Whitney, B., Churchwell, E., & Linz, H.: 2002, *ApJ* **579**, L95
- Hong, J., Schlegel, E. M., & Grindlay, J. E.: 2004, *ApJ* **614**, 508
- Kamata, Y., Koyama, K., Tsuboi, Y., & Yamauchi, S.: 1997, *PASJ* **49**, 461
- Kenyon, S. J. & Hartmann, L.: 1995, *ApJS* **101**, 117
- Knöldlseder, J.: 2000, *A&A* **360**, 539
- Luo, D., McCray, R., & Mac Low, M.-M.: 1990, *ApJ* **362**, 267
- Maggio, A., Sciortino, S., Vaiana, G. S., Majer, P., Bookbinder, J., Golub, L., Harnden, Jr., F. R., & Rosner, R.: 1987, *ApJ* **315**, 687
- Marino, A., Micela, G., Peres, G., & Sciortino, S.: 2003, *A&A* **407**, L63
- Massey, P. & Johnson, J.: 1993, *AJ* **105**, 980
- Meyer, M. R., Calvet, N., & Hillenbrand, L. A.: 1997, *AJ* **114**, 288
- Montmerle, T., Grosso, N., Tsuboi, Y., & Koyama, K.: 2000, *ApJ* **532**, 1097
- Morrell, N. I., Barbá, R. H., Niemela, V. S., Corti, M. A., Albacete Colombo, J. F., Rauw, G., Corcoran, M., Morel, T., Bertrand, J.-F., Moffat, A. F. J., & St-Louis, N.: 2001, *MNRAS* **326**, 85
- Morrison, R. & McCammon, D.: 1983a, *ApJ* **270**, 119
- Morrison, R. & McCammon, D.: 1983b, *ApJ* **270**, 119
- Nelan, E. P., Walborn, N. R., Wallace, D. J., Moffat, A. F. J., Makidon, R. B., Gies, D. R., & Panagia, N.: 2004, *AJ* **128**, 323
- Niemela, V. S., Morrell, N. I., Fernández Lajús, E., Barbá, R., Albacete Colombo, J. F., & Orellana, M.: 2006, *MNRAS* **367**, 1450
- Owocki, S., Townsend, R., & Ud-Doula, A.: 2005, in E. M. de Gouveia dal Pino, G. Lugones, & A. Lazarian (eds.), *AIP Conf. Proc. 784: Magnetic Fields in the Universe: From Laboratory and Stars to Primordial Structures.*, pp 239–252
- Owocki, S. P. & Cohen, D. H.: 1999, *ApJ* **520**, 833
- Pittard, J. M. & Stevens, I. R.: 2002, *A&A* **388**, L20
- Predehl, P. & Schmitt, J. H. M. M.: 1995, *A&A* **293**, 889
- Preibisch, T.: 2003, *A&A* **401**, 543
- Preibisch, T. & Feigelson, E. D.: 2005, *ApJS* **160**, 390
- Preibisch, T., Kim, Y.-C., Favata, F., Feigelson, E. D., Flaccomio, E., Getman, K., Micela, G., Sciortino, S., Stassun, K., Stelzer, B., & Zinnecker, H.: 2005, *ApJS* **160**, 401
- Press, W. H., Teukolsky, S. A., Vetterling, W. T., & Flannery, B. P.: 1992, *Numerical recipes in FORTRAN. The art of scientific computing*, Cambridge: University Press, —c1992, 2nd ed.
- Prestwich, A. H., Irwin, J. A., Kilgard, R. E., Krauss, M. I., Zezas, A., Primini, F., Kaaret, P., & Boroson, B.: 2003, *ApJ* **595**, 719
- Sanchawala, K., Chen, W.-P., Lee, H.-T., Chu, Y.-H., Nakajima, Y., Tamura, M., Baba, D., & Sato, S.: 2007, *ApJ* **656**, 462
- Schulz, N. S., Canizares, C., Huenemoerder, D., & Tibbets, K.: 2003, *ApJ* **595**, 365
- Schulz, N. S., Hasinger, G., & Truemper, J.: 1989, *A&A* **225**, 48
- Schulz, N. S., Testa, P., Huenemoerder, D. P., Ishibashi, K., & Canizares, C. R.: 2006, *ApJ* **653**, 636
- Seward, F. D. & Chlebowski, T.: 1982, *ApJ* **256**, 530
- Seward, F. D., Forman, W. R., Giacconi, R., Griffiths, R. E., Harnden, Jr., F. R., Jones, C., & Pye, J. P.: 1979, *ApJ* **234**, L55
- Siess, L., Dufour, E., & Forestini, M.: 2000, *A&A* **358**, 593
- Smith, N.: 2006, *MNRAS* **367**, 763
- Smith, N., Bally, J., & Morse, J. A.: 2003, *ApJ* **587**, L105

- Smith, N., Barbá, R. H., & Walborn, N. R.: 2004, *MNRAS* **351**, 1457
- Smith, N., Egan, M. P., Carey, S., Price, S. D., Morse, J. A., & Price, P. A.: 2000, *ApJ* **532**, L145
- Smith, R. K., Brickhouse, N. S., Liedahl, D. A., & Raymond, J. C.: 2001, *ApJ* **556**, L91
- Stevens, I. R., Blondin, J. M., & Pollock, A. M. T.: 1992, *ApJ* **386**, 265
- Tapia, M., Roth, M., Vázquez, R. A., & Feinstein, A.: 2003, *MNRAS* **339**, 44
- Townsley, L. K.: 2006, *ArXiv Astrophysics e-prints*
- Vuong, M. H., Montmerle, T., Grossi, N., Feigelson, E. D., Verstraete, L., & Ozawa, H.: 2003, *A&A* **408**, 581
- Walborn, N. R.: 1995, in V. Niemela, N. Morrell, & A. Feinstein (eds.), *Revista Mexicana de Astronomía y Astrofísica Conference Series*, Vol. 2 of *Revista Mexicana de Astronomía y Astrofísica*, vol. 27, pp 51–+
- Walter, F. M.: 1992, *AJ* **104**, 758
- Weisskopf, M. C., Brinkman, B., Canizares, C., Garmire, G., Murray, S., & Van Speybroeck, L. P.: 2002, *PASP* **114**, 1
- Wolk, S. J., Harnden, Jr., F. R., Flaccomio, E., Micela, G., Favata, F., Shang, H., & Feigelson, E. D.: 2005, *ApJS* **160**, 423
- Zhekov, S. A. & Skinner, S. L.: 2000, *ApJ* **538**, 808